



**HAL**  
open science

# A comparison of semi-Lagrangian Vortex method and Lattice Boltzmann method for incompressible flows

Chloé Mimeau, Simon Marié, Iraj Mortazavi

► **To cite this version:**

Chloé Mimeau, Simon Marié, Iraj Mortazavi. A comparison of semi-Lagrangian Vortex method and Lattice Boltzmann method for incompressible flows. *Computers and Fluids*, 2021, 224, pp.104946. 10.1016/j.compfluid.2021.104946 . hal-03214005

**HAL Id: hal-03214005**

**<https://hal.science/hal-03214005v1>**

Submitted on 9 May 2023

**HAL** is a multi-disciplinary open access archive for the deposit and dissemination of scientific research documents, whether they are published or not. The documents may come from teaching and research institutions in France or abroad, or from public or private research centers.

L'archive ouverte pluridisciplinaire **HAL**, est destinée au dépôt et à la diffusion de documents scientifiques de niveau recherche, publiés ou non, émanant des établissements d'enseignement et de recherche français ou étrangers, des laboratoires publics ou privés.



Distributed under a Creative Commons Attribution - NonCommercial 4.0 International License

# A comparison of semi-Lagrangian Vortex method and Lattice Boltzmann method for incompressible flows

Chlo Mimeau<sup>a,c</sup>, Simon Mari<sup>a,b</sup>, Iraj Mortazavi<sup>a,c</sup>

<sup>a</sup>*Conservatoire National des Arts et Mtiers, 2 rue Cont 75003 Paris, France*

<sup>b</sup>*Laboratoire DynFluid*

<sup>c</sup>*Laboratoire M2N*

---

## Abstract

The semi-Lagrangian Vortex method (VM) and the Lattice Boltzmann method (LBM) are used to investigate flows simulations in the incompressible regime. In this study, a proven version of each method is used and compared on different three dimensional benchmarks in terms of numerical accuracy, convergence, numerical diffusion and dissipation. The first comparisons are made on a convected vortex to study and compare the numerical dissipation of LBM and VM. Then the Taylor-Green vortex is investigated to compare the dissipation rate of the kinetic energy of each method. It is shown that both methods converge to the same solution but in a different way. The VM performs better than the LBM for the lowest resolution whereas LBM appears to be more accurate for the growing resolutions. These results are confirmed on 3D simulations with wall boundaries for the stiff test case of the wake behind a 3D cube at  $Re = 290$  and  $Re = 570$ .

*Keywords:* Vortex Methods, Lattice Boltzmann, Comparison, Numerical simulation, method accuracy, Taylor-Green Vortex, flow around a cube

---

## 1 Introduction

2 The design of numerical methods to study fluid flows has had a tremendous development during  
3 past decades. A large family of these methods such as finite difference, finite volume or finite  
4 element approaches as well as spectral/pseudo-spectral methods that deal with primitive variables  
5 and purely Eulerian frameworks, have been extensively studied both from consistency/stability  
6 point of view as well as numerical diffusivity and dissipation characterization. The later aspect  
7 is important to explore how numerical methods discretization properties affect the numerical  
8 efficiency and robustness and is highly dependent on the link between the scheme and the grid.

9 Two other classes of methods, namely Lattice Boltzmann and particle approaches, have met a  
10 large development recently in the context of incompressible or weakly-compressible flows. **The**

---

<sup>0</sup>**Abbreviations:** LBM, Lattice Boltzmann Method; VM, Vortex Method



11 first and major common thread shared by these two methods relies on the fact that they intrin-  
12 sically differ from the traditional approaches previously cited. In particular they do not directly  
13 deal with primitive variables contrary to previous methods and, in particular, the pressure field is  
14 not directly computed in their primary discretization. Moreover, they shortcut the non-linearities  
15 related to the advection phenomenon. For these reasons, they represent for many flow problems  
16 a promising alternative of software design. Now, if one considers Lattice Boltzmann and particle  
17 approaches with respect to each other, they interestingly show complementary aspects: indeed,  
18 on one side Lattice Boltzmann methods lie on a mesoscopic approach: they follow the evolution  
19 of probability distribution functions of fluid particles, thank to a fixed lattice, instead of calcu-  
20 lating the usual macroscopic variables involved in Navier-Stokes equations. On the other side,  
21 particle methods are Lagrangian approaches: the particles, playing the role of discretization  
22 elements and computational "points", move with the material velocity and the evaluation of  
23 the macroscopic quantities are evaluated on these numerical particles. Lattice Boltzmann is a  
24 mesoscopic Eulerian approach, whereas particle methods are macroscopic and Lagrangian. A  
25 recent focus on this kind of approaches has been investigated [1] for Lattice Boltzmann and SPH  
26 (Smoothed Particle Hydrodynamics) methods to solve 2D problems in multiphase flows, which  
27 demonstrates the current interest of such type of alternative and non-traditional methods.

28 The present work aims at describing and comparing a semi-Lagrangian Vortex particle method  
29 and a Lattice Boltzmann method, in order to try to numerically highlight the above statements  
30 in the case of various physical 3D problems in CFD (Computational Fluid Dynamics). All the  
31 computations made in this study are based on in-house and research codes, developed or co-  
32 developed by the authors of the present paper.

33 Vortex methods (VM) belong to particle methods. They are based on a Lagrangian or semi-  
34 Lagrangian description of the governing equations (Euler equations, linear convection-diffusion  
35 equation, Navier-Stokes equations) which, when they are resolved, provide the dynamics and  
36 the evolution of the fluid elements. In the case of Vortex methods, the fluid elements are nu-  
37 merical particles, characterized by their spacial position and the vorticity they carry. With the  
38 first vortex sheet computations in the 1930s [2, 3], the Vortex methods correspond to one of the  
39 first numerical method ever used in the Computational Fluid Dynamics community. This can  
40 be explained by their very natural framework provided by the particle approach, mimicking the  
41 physics, which make them particularly well suited for advection dominated flow problems in par-  
42 ticular because the Lagrangian treatment of the convective term is free of numerical dissipation.  
43 In the 70s, a lot of efforts have been devoted to propose numerical developments that overcome  
44 the main intrinsic difficulties of Lagrangian Vortex methods, mostly relying on the modeling of  
45 the viscous effects in Navier-Stokes equations [4, 5] and the treatment of boundary conditions  
46 [6]. Significant developments were also made in the last decade in order to provide to Lagrangian  
47 Vortex methods (also called Particle Vortex methods) an efficient evaluation of the velocity field.  
48 Indeed, for  $N_p$  particles in the computational domain, the classical resolution of the Biot-Savart  
49 law (which gives the velocity from the vorticity) implies to compute the interactions between all  
50 the particles, leading to a  $\mathcal{O}(N_p^2)$  computational cost. The development of the Fast Multipole  
51 Method (FMM) allowed to drastically reduce the cost of such operation [7, 8, 9, 10, 11]. More-  
52 over, the issue related to the distortion of the particle distribution, which is one of the major  
53 drawback of pure Lagrangian methods, has been subject to deep researches in order to design

54 accurate Particle Vortex methods preventing from high clustering or rarefaction of the vortex  
55 particles in the domain [10, 12, 13].

56 Thanks to the remeshing technique introduced in the 90s [14, 15], it exists another main vari-  
57 ant of Vortex methods, which relies on a semi-Lagrangian approach. The remeshing technique  
58 was originally proposed to bypass the inherent problem of the distortion of Lagrangian particle  
59 distribution. It consists in periodically redistributing the particles onto an underlying Cartesian  
60 grid in order to ensure their overlapping and thus the convergence of the solution. Following the  
61 introduction of this remeshing procedure, semi-Lagrangian Vortex methods emerged, also called  
62 remeshed Vortex methods (or Vortex Particle-Mesh method or Vortex-in-Cell method). They  
63 are characterized by the fact that the vorticity transport equations and the velocity equation are  
64 both handled on the particles field and on a Cartesian grid. They allow one to benefit from the  
65 strengths of Particle Vortex schemes to handle the flow advection and from the one of grid-based  
66 methods, like immersed boundary methods to model boundary conditions or FFT to solve the  
67 Poisson equation. Based on these different improvements, Vortex methods have matured and  
68 now offer a robust framework able to compete with pure Eulerian methods in the handling of  
69 challenging problems like interface tracking for colliding obstacles [16], fluid-structure interaction  
70 [17, 18, 19], shape optimization [20], flows past bluff bodies [19], passive control using porous  
71 media [21], wind turbine aerodynamics [22] or reinforcement learning [23]. In the present study,  
72 the VM denomination will be restricted to the remeshed (semi-Lagrangian) Vortex method. All  
73 the VM simulations presented in this work are based on an in-house parallel and object-oriented  
74 library, implemented in Python/Fortran language.

75 The Lattice Boltzmann Method [24, 25] (LBM) is nowadays recognized as a fast and reliable  
76 algorithm to numerically solve the Boltzmann equation. The physics of this kind of model is  
77 led by a mesoscopic description of the collision between particles. Hence, if a given collision  
78 operator is chosen with a reliable equilibrium state, a wide variety of physical modeling could be  
79 obtained, from turbulent to relativistic flows [26, 27, 28]. In order to describe fluid dynamics,  
80 governed by the Navier-Stokes equation, the BGK collision operator, based on a relaxation  
81 towards the equilibrium, has been shown to be an efficient mesoscopic description [29]. The  
82 Lattice Boltzmann methods then perform a discretization of the velocity space in which the fluid  
83 particles are allowed to displace. This discretization has to be highly connected to the mesh  
84 and induces strong constraints in the choice of the velocity lattice. These constraints are often  
85 coupled to the algorithmic advection which basically relies on a collision and a propagation step.  
86 The propagation step is led by the mesh and the collision step depends on the description of the  
87 relaxation process. The traditional way to describe this step is to assign a relaxation parameter  
88 to the main statistical moments when they relax to their equilibrium state. This model, also  
89 referred to as *MRT* model for Multiple Relaxation Times [30] has been shown to recover the  
90 behavior of the weakly compressible Navier-Stokes equation. It has been shown [31, 32] that this  
91 kind of method has a lower dissipation error compared to traditional finite-difference schemes.  
92 As a counterpart, LBM suffers from numerical instabilities when Reynolds number becomes  
93 high. The origins of LBM instabilities have been actively studied and remain an open subject  
94 [33, 34, 35]. Some modern collision models have now emerged and could improve those aspects  
95 by changing the moments definition [36], by re-normalizing the post-collision step [37], or by  
96 enforcing energy conservation [38, 39, 40]. A theoretical comparison of a wide variety of collision

97 models has been recently reviewed in [41, 35]. In the present study, the LBM method will be  
 98 restricted to the standard *MRT* model with optimized relaxation times defined in [30]. All the  
 99 LBM simulations exposed in this work are based on this approach, which is implemented in a  
 100 proper in-house parallel scientific Python/Fortran code.

101 Despite their increasing applications, the Lattice Boltzmann and Vortex methods suffer from  
 102 a lack of extensive computational characterization in the literature (dissipation, diffusivity, pa-  
 103 rameter dependency, etc.) and deserve a better focus on such issues. This paper is devoted to  
 104 the numerical characterization of a Lattice Boltzmann and a remeshed Vortex method. On one  
 105 hand this work aims at enlightening the effect of the time and space discretization refinement on  
 106 the accuracy and robustness of these techniques and on the other hand at clarifying their grid  
 107 vulnerability with a quantitative evaluation of the numerical diffusion and dissipation. Finally,  
 108 this study is an attempt to classify the strong and weak points of both methods in order to offer  
 109 an understanding of their range of efficiency.

110 This paper is organized as follows, the first section is dedicated to the presentation of some  
 111 basic theoretical background of each method, where the differences and similarities of LBM and  
 112 VM algorithms are clearly highlighted and discussed. Then, in section 2, the two methods are  
 113 compared in terms of numerical dissipation on classical test cases : first, the simulation of a  
 114 simple convected vortex is investigated in a 3D periodic domain and then the three-dimensional  
 115 Taylor-Green vortex flow is performed, followed by a discussion on the evolution of enstrophy and  
 116 kinetic-energy. Then, section 3 discusses the effect of wall boundary condition for each method  
 117 on the three-dimensional flow past a cube at different Reynolds numbers.

## 118 1. Theoretical backgrounds

### 119 1.1. Vortex method

#### 120 1.1.1. Governing equations

Vortex methods are based on the velocity-vorticity formulation of the incompressible Navier-Stokes equations in a domain  $D$ , which reads:

$$\frac{\partial \boldsymbol{\omega}}{\partial t} + (\mathbf{u} \cdot \nabla) \boldsymbol{\omega} - (\boldsymbol{\omega} \cdot \nabla) \mathbf{u} = \frac{1}{Re} \Delta \boldsymbol{\omega} \quad \text{in } D. \quad (1)$$

In this equation  $\boldsymbol{\omega}$ ,  $\mathbf{u}$  and  $Re$  respectively denote the vorticity, the velocity and the Reynolds number. The first term corresponds to the advection of the vorticity  $\boldsymbol{\omega}$  carried by the particles at the velocity  $\mathbf{u}$ . The second non-linear term  $(\boldsymbol{\omega} \cdot \nabla) \mathbf{u}$  models the stretching of the flow structures (it vanishes in 2D) and the right hand side term represents the diffusion of  $\boldsymbol{\omega}$  under viscous effects. This equation has to be coupled to the system giving the velocity in terms of the vorticity. Using the incompressibility condition, the velocity may be directly linked to the vorticity through the following Poisson equation:

$$\Delta \mathbf{u} = -\nabla \times \boldsymbol{\omega}. \quad (2)$$

121 The system (1)-(2) has to be complemented by appropriate boundary conditions at artificial  
 122 boundaries and at solid boundaries (if present). The prescription of such solid boundary condition

123 may be done by adding a forcing term in the right hand side of equation (1). This issue will be  
 124 specifically addressed in section 3.

### 125 1.1.2. Discretization method

126 To solve the  $(\boldsymbol{\omega}, \mathbf{u})$  Navier-Stokes equations (1)-(2), the flow is discretized onto particles that  
 127 carry the vorticity field  $\boldsymbol{\omega}$  transported at the velocity  $\mathbf{u}$  and the resolution of the governing  
 128 equations is based on a splitting algorithm, which consists at each time step in successively  
 129 solving the following equations:

$$\Delta \mathbf{u} = -\nabla \times \boldsymbol{\omega} \quad (3)$$

$$\frac{\partial \boldsymbol{\omega}}{\partial t} = \text{div}(\boldsymbol{\omega} : \mathbf{u}) \quad (4)$$

$$\frac{\partial \boldsymbol{\omega}}{\partial t} = \frac{1}{Re} \Delta \boldsymbol{\omega} \quad (5)$$

$$\frac{\partial \boldsymbol{\omega}}{\partial t} + (\mathbf{u} \cdot \nabla) \boldsymbol{\omega} = 0 \quad (6)$$

$$\Delta t_{\text{adapt}} = \frac{\text{LCFL}}{\|\nabla \mathbf{u}\|_{\infty}} \quad (7)$$

The discretization of each equation of this fractional step algorithm is realized in this study by using a remeshed vortex method.

The advection of vorticity field (eq. (6)) is performed in a Lagrangian way using a vortex method:

$$\left\{ \begin{array}{l} \frac{dx_p}{dt} = u_j^n(x_p), \quad j \in \{1, 2, 3\} \\ x_p^n = x_i^n, \\ \frac{d\omega_p}{dt} = 0, \\ \omega_i^{n+1} = \sum_p \omega_p^n \Lambda_{4,2} \left( \frac{x_p^{n+1} - x_i}{h} \right) \end{array} \right. \quad \begin{array}{l} \text{(advection)} \\ \\ \\ \text{(remeshing)} \end{array} \quad (8)$$

At each time step of the method, numerical particles are created on the nodes  $i$  of an underlying uniform Cartesian grid ( $x_p^n = x_i^n$ ) and the new position  $x_p^{n+1}$  of each particle  $p$  is obtained by solving  $d_t x_p = u_j^n(x_p)$ , while the transported vorticity remains constant ( $d_t \omega_p = 0$ ). This Lagrangian treatment of the advection step is close to the physics and provides a flexible resolution of the non-linearities, decreasing drastically the numerical diffusion. In this work, we numerically integrate the particle positions in time ( $d_t x_p = u_j^n(x_p)$ ) by using an explicit 2<sup>nd</sup> order Runge-Kutta method. The only difficulty of this step relies on the interpolation of the velocity field at the intermediate position of the particles in the RK2 scheme, since this intermediate position will not always be aligned with the grid. In the present case, it is performed by using bilinear interpolation.

Once the particle positions  $x_p$  have been updated according to the flow velocity, the vorticity carried by each particle is redistributed on the neighbouring points of the underlying Cartesian

grid using a remeshing kernel of type  $\Lambda_{p,r}$  [42] (cf last equation of system (8)). The  $\Lambda_{p,r}$  remeshing kernels are piecewise polynomial functions of regularity  $\mathcal{C}^r$ , satisfying the conservation of the first  $p$  moments. The one used in this work is  $\Lambda_{4,2}$ : this kernel is of regularity  $\mathcal{C}^2$ , it satisfies the conservation of 4 moments and includes 6 grid points by direction in its support on which each particle can be redistributed. In this work, the particle advection and the remeshing procedure are performed using a directional splitting approach [43]. It consists in successively solving 1D convection/remeshing problems, direction by direction, as written in eqs. (8). This directional splitting allows to save significant computational efforts compared to a classical tensorial approaches, especially in 3D.

The systematic remeshing of particles onto an Eulerian grid at each time step after the advection stage (eq. (6)), enables to ensure the overlapping of particles required for the convergence of the method. Moreover the presence of the grid allows to discretize the other equations using efficient and/or fast grid methods (finite differences and spectral method based on FFT evaluations). In the present algorithm, equations (3) to (5) are solved on the grid.

The Poisson equation (3) is resolved in the Fourier space with periodic boundary conditions according to the following expression :

$$\widehat{\mathbf{u}}(\xi) = \frac{1}{|\xi|^2} (\widehat{\nabla \times \boldsymbol{\omega}}) \quad (9)$$

130 In the presence of an underlying mesh that is uniform and Cartesian (like in the present VM), the  
 131 use of FFT-based evaluations for the velocity computation may be considered as one of the most  
 132 appropriate and efficient approach [44, 45]. However, if the grid is non-uniform then the use of  
 133 other type of algorithm is mandatory. In that case, the most famous and efficient one, which is  
 134 widely used in meshless (i.e. purely Lagrangian) Vortex methods [46, 11], is the Fast Multipole  
 135 Method (FMM) like in the works dealing with adaptive mesh refinement (AMR) [47, 48].

Regarding the stretching problem (4), it is considered here in its conservative formulation:

$$\frac{\partial \boldsymbol{\omega}}{\partial t} = \text{div}(\boldsymbol{\omega} : \mathbf{u}), \quad (10)$$

where  $\text{div}(\boldsymbol{\omega} : \mathbf{u}) := (\boldsymbol{\omega} \cdot \nabla) \mathbf{u} + \mathbf{u} \text{div}(\boldsymbol{\omega})$ . The time integration scheme chosen here to discretize this equation is the 3<sup>rd</sup> order Runge-Kutta scheme. Throughout this time discretization, the velocity field involved in the divergence operator is not modified. The divergence operator is discretized through a 4<sup>th</sup> order centered finite-differences scheme on the grid.

Concerning the diffusion equation (5), it is discretized in time using an implicit 1<sup>st</sup> order Euler scheme and then solved in the Fourier space.

An adaptive time-step  $\Delta t_{\text{adapt}}$  (7) is computed at the end of the fractional step algorithm. It is based on the non-linear stability of the advection/remeshing scheme in Vortex methods:

$$\Delta t_{\text{adv}} \leq \frac{\text{LCFL}}{\|\nabla \mathbf{u}\|_{\infty}}, \quad (11)$$

136 where the LCFL denotes the Lagrangian CFL [49]. This number must satisfy  $\text{LCFL} < 1$  [42],  
 137 which, from a physical point of view, imposes that particles trajectories do not cross. As the time

138 step defined by this stability condition (11) is not constrained by the grid size or the distance  
 139 between the particles but only by the flow strain, it often provides larger time steps compared  
 140 to Eulerian schemes, based on CFL conditions.

141 Table 1 summarizes the time and space discretization schemes used in this work to solve each  
 142 equation of the present fractional step algorithm.

| Equation               | Time discretization method    | Space discretization method                  |
|------------------------|-------------------------------|--|
| Poisson equation (3)   | -                             | spectral method                              |
| Stretching (4)         | RK3 scheme                    | 4 <sup>th</sup> order centered FD            |
| Diffusion (5)          | implicit Euler scheme         | spectral method                              |
| Advection + Remesh (8) | RK2 scheme (particles advec.) | remeshing with $\Lambda_{4,2}$ kernel        |
| Adaptive time step (7) | -                             | 4 <sup>th</sup> order centered FD (LCFL < 1) |

Table 1: Time and space discretization methods used for the resolution of the viscous splitting VM algorithm (eqs. (3) to (7)).

143 The fractional construction of this algorithm offers a flexibility in the choice of the discretization  
 144 schemes of each step. The algorithm exposed in this work is one of the different existing remeshed  
 145 vortex algorithms in literature. We can cite for instance the remeshed vortex algorithms used  
 146 in [50] and [16], which differ from the present one by the nature of the remeshing kernel ( $\Lambda_{2,1}$   
 147 instead of  $\Lambda_{4,2}$  here), by a tensorial approach for the advection/remeshing step (contrary to the  
 148 directional one proposed here), or by the use of a centered fourth-order [50] or second-order [16]  
 149 finite differences scheme for the evaluation of the viscous term. In the algorithm established by  
 150 [22], the main difference with respect to [50, 16] or the present one relies on the fact that the  
 151 remeshing operation is not performed every time step but only every 5 time steps (using a  $\Lambda_{2,1}$   
 152 kernel, with a tensorial approach). This choice implies a particle-to-mesh and a mesh-to-particle  
 153 interpolation operation for the time steps where remeshing is not applied.

154 Providing the stability and consistency of all the numerical schemes used in each sub-steps,  
 155 remeshed Vortex method algorithms are proved to converge numerically as shown in the above  
 156 literature reference and as it will be highlighted in the next sections of this paper.

## 157 1.2. Lattice Boltzmann method

The Lattice Boltzmann method [24], used to perform fluid flow simulations, is not directly  
 based on the resolution of the Navier-Stokes equations but is a particular discretization of the  
 Boltzmann equation, describing the dynamics of gas:

$$\frac{\partial f(\mathbf{c}, \mathbf{x}, t)}{\partial t} + c_i \frac{\partial f(\mathbf{c}, \mathbf{x}, t)}{\partial x_i} = \left( \frac{\partial f}{\partial t} \right)_{\text{coll}} \quad (12)$$

158 where  $f(\mathbf{c}, \mathbf{x}, t)$  is the distribution of particles density with a given velocity  $\mathbf{c}$  at a given position  
 159  $\mathbf{x}$  at time  $t$ . The left hand side terms corresponds to the propagation (advection) of the particles  
 160 and the right hand side term represents the time evolution of the distribution function  $f$  due  
 161 to the collisions between particles. In this work, the collision between particles is given by the

162 BGK [29] collision operator which describes an average collision effect through the relaxation to  
 163 a local equilibrium  $f^{eq}$  with a relaxation parameter  $\tau$ :

$$\frac{\partial f(\mathbf{c}, \mathbf{x}, t)}{\partial t} + c_i \frac{\partial f(\mathbf{c}, \mathbf{x}, t)}{\partial x_i} = -\frac{1}{\tau}(f - f^{eq}) \quad (13)$$

In order to solve (13) numerically, one should restrict the velocity space to a discrete one. This part is very important and gives the LBM its numerical originality. To perform this discretization, the standard Gauss quadrature is used and is detailed in [26]. The number of lattice points needed to achieve a given dynamics is directly connected to this latter step and converts  $f(\mathbf{c}, \mathbf{x}, t)$  into  $f(\mathbf{c}_\alpha, \mathbf{x}, t)$  where  $\alpha$  denotes the discrete velocities indices. The usual 19 velocities lattice (D3Q19) allows to recover the dynamics described by the 3D isothermal Navier-Stokes equations for small Mach numbers. From this lattice, one could define an equilibrium function in its incompressible polynomial form:

$$f_\alpha^{eq}(\mathbf{x}, t) = \rho\omega_\alpha + \rho_0\omega_\alpha \left( \frac{\mathbf{u} \cdot \mathbf{c}_\alpha}{\tilde{c}_0^2} + \frac{(\mathbf{u} \cdot \mathbf{c}_\alpha)^2}{2\tilde{c}_0^4} - \frac{|\mathbf{u}|^2}{2\tilde{c}_0^2} \right) \quad (14)$$

164 where  $\rho_0$  is a unity constant and the coefficients  $\omega_\alpha$  and  $\tilde{c}_0$  are defined by:

$$\begin{cases} \omega_\alpha = \frac{1}{3}, \frac{1}{18}, \frac{1}{36} & , \quad \alpha = 0, \alpha = 1..6, \alpha = 7..18 \\ \tilde{c}_0^2 = \frac{1}{3} \end{cases} \quad (15)$$

The macroscopic variables,  $\rho, \mathbf{u}$  are linked to the distribution functions  $f$  by their moments:

$$\begin{aligned} \rho &= \sum f_\alpha \\ \rho \mathbf{u} &= \sum_\alpha \mathbf{c}_\alpha f_\alpha \end{aligned} \quad (16)$$

165 Then, the final step to get the LBM algorithm is to perform a space and time discretization.  
 166 This is achieved by using the advective properties of the left-hand side of equation (13) which  
 167 can be integrated along the characteristic  $\mathbf{c}_\alpha$  to get the following LBM algorithm:

$$\begin{cases} g_\alpha^{coll}(\mathbf{x}, t) &= g_\alpha(\mathbf{x}, t) - \frac{dt}{\tau_g}(g_\alpha(\mathbf{x}, t) - g_\alpha^{eq}(\mathbf{x}, t)) \\ g_\alpha(\mathbf{x}, t) &= g_\alpha^{coll}(\mathbf{x} - \mathbf{c}_\alpha dt, t - dt) \end{cases} \quad (17)$$

168 where the  $g_\alpha$  distribution function comes from the integration step to get an explicit formulation  
 169 and is related to the distribution  $f_\alpha$  with the relation  $g_\alpha = f_\alpha + \frac{dt}{2\tau}(f_\alpha - f_\alpha^{eq})$  which implies  
 170  $g_\alpha^{eq} = f_\alpha^{eq}$  and  $\tau_g = \tau + \frac{dt}{2}$ .

From this, the algorithm imposes  $dt = dx = 1$  in order to be consistent with a uniform grid size imposed by the lattice. Then one could define some physical time and grid steps in order

to compute physical quantities from lattice quantities. This is done by introducing the physical speed of sound  $c_0$  which defines:

$$\Delta t = \frac{\tilde{c}_0 \Delta x}{c_0} \quad (18)$$

171 where  $\Delta x$  is the physical grid step obtained by discretizing a reference length scale  $L$  with a  
 172 given number of points  $N$ . Based on these parameters, the LBM algorithm can recover the  
 173 Navier-Stokes dynamics with a second-order accuracy in space and time.

174 In the BGK collision operator, the distribution functions relax toward the equilibrium according  
 175 to a single relaxation time. A more sophisticated idea is to relax each moment according to a  
 176 proper relaxation time. This method is called multiple relaxation time (MRT) [30] and is known  
 177 to alleviate some stability issues encountered with the BGK operator. The implementation of  
 178 the MRT model is based on the modification of the collision step of equation (17) which is done  
 179 in the momentum space:

$$\begin{cases} \mathbf{m}^{coll}(\mathbf{x}, t) &= \mathbf{m}(\mathbf{x}, t) - \mathcal{S}(\mathbf{m}(\mathbf{x}, t) - \mathbf{m}^{eq}(\mathbf{x}, t)) \\ \mathbf{g}(\mathbf{x}, t) &= \mathcal{M}^{-1} \mathbf{m}^{coll}(\mathbf{x} - \mathbf{c}_\alpha dt, t - dt) \end{cases} \quad (19)$$

where the matrix  $\mathcal{M}$ , transforms the distribution functions into moments:

$$\mathbf{m} = \mathcal{M} \mathbf{g}. \quad (20)$$

$\mathcal{M}$  is a square transformation matrix. If the first line of the matrix is filled only by 1, then the first moment is the density. The invert transformation from the moments to distribution functions is simply  $\mathbf{g} = \mathcal{M}^{-1} \mathbf{m}$ . Further details about the construction of the matrix  $\mathcal{M}$  can be found in [30]. The equilibrium moments are obtained from  $\mathbf{m}^{eq} = \mathcal{M} \mathbf{g}^{eq}$ . The diagonal of  $\mathcal{S}$  corresponds to the inverse of the relaxation time, also called relaxation rate, associated with each moment:

$$\mathcal{S} = \text{diag}(0, s_1, s_2, 0, s_3, 0, s_3, 0, s_3, s_\nu, s_2, s_\nu, s_2, s_\nu, s_\nu, s_\nu, s_4, s_4, s_4) \quad (21)$$

where  $s_\nu$  is related to the fluid viscosity:

$$\frac{1}{s_\nu} = 3\nu - \frac{1}{2} \quad (22)$$

180 The other relaxation rates,  $s_1, s_2, s_3$  and  $s_4$  do not appear in the macroscopic equations and are  
 181 chosen according to stability optimization [51, 30] leading to  $s_1 = 1.19, s_2 = 1.4, s_3 = 1.2, s_4 =$   
 182  $1.98$ . The BGK operator is recovered if all the relaxation rates are the same.

183 Then the LBM algorithm used in this study will rely on equations (14), (16) and (19), imposing  
 184 the physical parameters with (18) and (22). It is to be noticed that other forms of the collision  
 185 operator are possible [36, 37, 52, 53, 54, 55, 56] but would give very similar results for the test-  
 186 cases considered in this study. Moreover, a high order formulation of eq. (14) could be adopted  
 187 to enhance stability issues [57] and to reach higher Mach numbers [58]. **A detailed theoretical**  
 188 **comparison of the different collision models and their impact on the physics can be found in [41]**  
 189 **and [35]. Then, the massively used D3Q19 lattice with the MRT collision operator will serve as**  
 190 **the reference LBM model in the following comparisons.**



191 *1.3. Algorithmic comparison*

192 In order to summarize the theoretical backgrounds exposed in the previous sections, the basic  
 193 steps of each algorithm are detailed in Table 2.

| Step                         | LBM  | VM   |
|------------------------------|--|--|
| Initialization ( $t^* = 0$ ) | Compute $g_\alpha$ from $\rho$ and $\mathbf{u}$                    | Compute $\boldsymbol{\omega} = \nabla \times \mathbf{u}$ from $\mathbf{u}$ |
| RHS update                   | Collision from (19)-1  | Stretching (4) and diffusion of $\boldsymbol{\omega}$ (5)                  |
| Advection                    | Streaming from (19)-2  | Particles advection + remeshing (8)  |
| Macro state update           | Compute $\rho$ and $\mathbf{u}$ from $g_\alpha$<br>and update (14) | Compute $\mathbf{u}$ from $\boldsymbol{\omega}$ (3)                        |

Table 2: Comparison of the basic algorithmic steps for present LBM and VM methods.

194 In order to compare this two different kind of methods, some important features should be  
 195 pointed out. The computed quantities of each method are basically different. Indeed, LBM  
 196 computations compute the distribution functions and give direct access to density and velocity  
 197 whereas VM methods compute the vorticity and the velocity. Then because of the incompressible  
 198 nature of the VM, only velocity and vorticity will be compared in this study. The Mach number  
 199 of the LBM method will always be chosen to a low value and the equilibrium will be computed  
 200 with relation (14). Finally, it should be mentioned that the vorticity is not a native quantity in  
 201 the LBM algorithm and must be reconstructed. Then when a time evolution of the vorticity will  
 202 be needed in LBM computations, it will be reconstructed inside the algorithm with only second  
 203 order in space to preserve the global order of computation.

204 **Then, it should be highlighted that a fine computational cost comparison is delicate to handle**  
 205 **in the present study.** Indeed, these types of considerations are very dependent on the level of  
 206 implementation of the algorithms (pedagogic, academic, industrial, optimized) and should be  
 207 considered in a dedicated study. However, some basic features of the implementation can be  
 208 pointed out for each method (**they will be confirmed in section 2.1 with Table 3 giving indicative**  
 209 **CPU-times for a well chosen test case**). Concerning LBM, the classical implementation of the  
 210 algorithm is spread out into a local collision step which represents the main computational cost  
 211 and an advection step which is generally very fast due to the low stencil of the D3Q19 lattice.  
 212 The counterpart of this efficiency is that the LBM timestep is generally limited by the grid  
 213 step, meaning that it should be low for high resolution. Concerning VM, the computational  
 214 time dedicated to the resolution of the advection/remeshing step is also rather fast due to the  
 215 directional splitting (successive resolutions of 1D problems in each spacial direction), as well as  
 216 the resolution of the Poisson equation and diffusion (by using the optimized FFTW library). On  
 217 the other side, the resolution of the stretching equation and the evaluation of  $\Delta t_{\text{adapt}}$  represent  
 218 a non negligible part or the total computational time within one time step. However, the use of  
 219 such adaptive time step enables to significantly reduce the number of total iterations needed to  
 220 complete simulations, which leads to a net reduction of total computational time compared to  
 221 simulations based on classical CFL conditions.

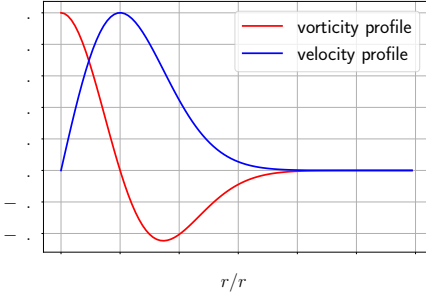
## 222 2. Numerical dissipation

223 In this section some standard test-case computations will be performed to characterize the level  
224 of numerical dissipation induced by each method. To investigate this kind of numerical char-  
225 acteristics, the linear stability analysis (LSA) of the scheme could be a powerful and efficient  
226 theoretical tool. The LSA of the LBM has been the purpose of numerous studies [59, 31, 60].  
227 The main conclusion of these studies relies on the low dissipation rate of the perturbative (or  
228 acoustic) mode due to the mesoscopic nature of the method and a level of numerical dissipation  
229 for the vorticity mode comparable to 3<sup>rd</sup> order of macroscopic method such as finite-differences.  
230 Concerning remeshed Vortex methods, according to the authors knowledge, there is no LSA or  
231 complete numerical analysis of convergence for fractional step algorithms like the one used in  
232 this paper (cf Tab. 1) due to its heterogeneous aspect. However, it is important to mention the  
233 theoretical studies carried out in the pure Lagrangian framework of the Vortex methods: Hald  
234 in 1979 [61] and then Beale and Majda in 1982 [62] proved the theoretical convergence of pure  
235 Lagrangian Vortex methods in the context of the 2D Euler equations (inviscid flows). Later,  
236 the time discretization was added in the convergence analysis of the 2D and 3D Euler equations  
237 by Anderson and Greengard in 1985 [63]. Besides the existence of a theoretical convergence  
238 analysis, a very interesting feature of Lagrangian Vortex methods relies on the fact that they  
239 conserve many inviscid flow invariants. For the 2D Euler equations, Vortex methods guarantee  
240 the conservation of 4 invariants, namely the total circulation, the linear and angular impulses as  
241 well as the kinetic energy, as proved in [64]. The conservation properties of Lagrangian Vortex  
242 methods ensure that they are naturally free of numerical dissipation which implies that, even  
243 for underresolved simulations, they provide correct qualitative solutions. Concerning the semi-  
244 Lagrangian aspect of the method and the particle remeshing, Cottet et. al [42] proved recently  
245 the consistency and linear stability of the advection/remeshing scheme (eqs. (8)) with remeshing  
246 kernels  $\Lambda_{p,r}$  until  $p = 8$ .

247 A relative comparison of the present LBM and remeshed VM on well-known test cases will  
248 therefore give some insight on the numerical dissipation induced by these non fully macroscopic  
249 methods.

### 250 2.1. Advection of a simple vortex

251 For this first test case, the simple and widely used Taylor vortex is investigated. Here, the con-  
252 vection of a viscous vortex is used to characterize the effects of each discretization strategies on  
253 the dissipation of a simple coherent structure. For this test case, a periodic  $[L, L, L/4]$  domain  
254 is used and the velocity field is initialized by equations (23) where  $r^2 = (x - x_0)^2 + (y - y_0)^2$ ,  
255  $r_0 = L/10$  and  $U_t = U_\infty/10$ . The LBM pressure is initialized so as to ensure the isotropic condi-  
256 tion and avoid some spurious oscillations. This latter point is particularly discussed in dedicated  
257 publications [65, 66]. The Taylor vortex has the particularity to be surrounded by a negative  
258 vorticity region between  $r = r_0$  and  $r = 4r_0$ . Moreover, the velocity profile has a compact form  
259 and reaches a very small value for  $r > 4r_0$  (Fig. 1). For this first comparison, all the numerical  
260 parameters such as grid size and time-step will be the same for both LBM and VM. Then in order  
261 to get rid of the peculiar normalization procedure of each method and for the sake of clarity,



$$\begin{cases} u_x &= U_\infty - \frac{U_t}{r_0}(y - y_0) \exp\left[\frac{1}{2}\left(1 - \frac{r^2}{r_0^2}\right)\right] \\ u_y &= \frac{U_t}{r_0}(x - x_0) \exp\left[\frac{1}{2}\left(1 - \frac{r^2}{r_0^2}\right)\right] \\ u_z &= 0 \end{cases} \quad (23)$$

Figure 1: Velocity and vorticity profiles of the convected Taylor vortex.

the vortex will be defined in physical units. Thus, the characteristic dimensions are taken to  $U_\infty = 34\text{m/s}$  and  $L = 1.28\text{m}$ . The Reynolds number based on  $r_0$  is set to 100 in order for the diffusion term to be effective in the VM algorithm. Indeed, this test case is usually performed in the inviscid form to get rid of the viscous dissipation and directly compare the numerical dissipation. But for the present study, the numerical schemes are compared in the three presented test cases with all the features described in Table 2. From these parameters, the grid size is set to  $\Delta x = L/N$  where  $N$  is the grid resolution and the time-step is chosen so as to enforce a CFL number based on the upstream velocity  $\text{CFL} = U_\infty \frac{\Delta t}{\Delta x} = 1/\sqrt{3} \approx 0.057$  for both LBM and VM models.

The center of the vortex is initially positioned at the center of the 3D periodic  $[L, L, L/4]$  domain and its convection is observed through a given number of domain crossings while the grid resolution  $N \times N \times N/4$  in the whole domain is varying from  $N = 16$  to 256. **Concerning the present VM, since it is a semi-Lagrangian Vortex method, one recalls that at each time step of the algorithm the particles are redistributed on the background grid nodes and then convected in a Lagrangian way (cf eqs 8), thus implying that the total number of particles in the domain is always equal to the underlying grid resolution.**

The velocity and vorticity signals recorded in the center point of the domain are plotted on Figures 2, 3 and 4 with respect to the normalized time  $t^* = tU_\infty/L$ .

First of all, the convergence behavior is clearly different in VM and LBM. Indeed, from Figure 2, one can see that the coarse resolution underestimates the LBM velocity whereas it is overestimated with VM. The LBM results exhibit a large dispersion for coarse resolution.

Then, it should be noticed that the LBM vorticity is a reconstructed quantity which explains that the initial vorticity for the lowest resolution is slightly lower than the theoretical one because of the second order reconstruction (see the solid blue curve at  $t^* = 0$  on Fig. 3). Thus the vorticity level for the LBM results at the lowest resolution should be interpreted with this initial reconstruction error. Then the first global results of Figure 3 clearly show a similar behavior for LBM and VM results. The stronger difference is observed for the lowest resolution where the LBM results exhibit a higher numerical dispersion of the convected vortex, which is not at the expected position. The close-up view of Figure 4 highlights that the VM vortex has less dispersion for the overall resolutions.

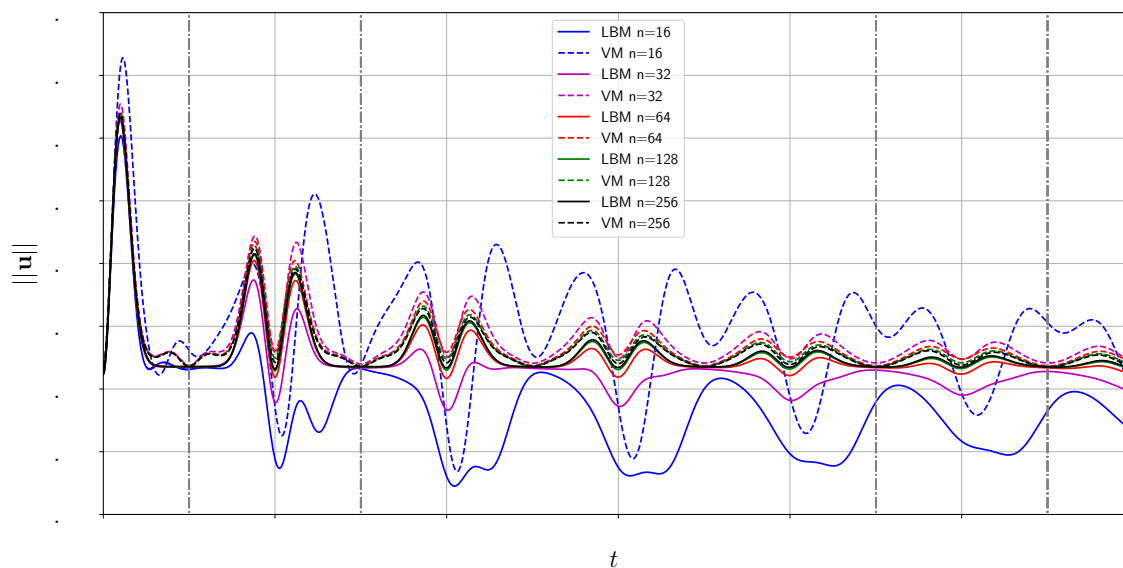


Figure 2: Time evolution of the velocity norm at the center of the computational domain.

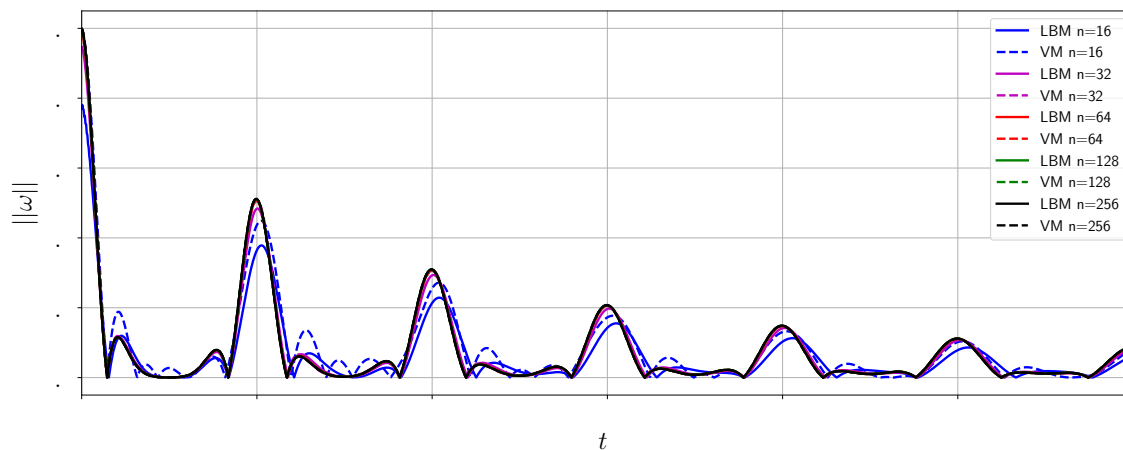


Figure 3: Time evolution of the vorticity norm at the center of the computational domain.

292 The comparisons of the vortex shapes in Figure 5 confirm these observations by highlighting a  
 293 strong deformation of the LBM vortex for the lowest resolution after 2 domain-crossings (second  
 294 column of Fig. 5). Then the vortex dissipates and the limit of the negative vorticity ring reaches  
 295 the end of the domain (last column of Fig. 5). We note that the vortex shapes obtained for both  
 296 methods with  $N = 256$  do not show qualitative change compared to the case  $N = 128$  and are  
 297 consequently not represented in Figure 5.

To take into account the overall results for both velocity and vorticity, the evolution of the numerical dissipation with the numerical wavenumber is shown in Figure 6. This dissipation rate  $G$  is estimated by averaging the norm of the desired quantity  $\mathbf{q}$  during the period  $T = L/U_\infty$

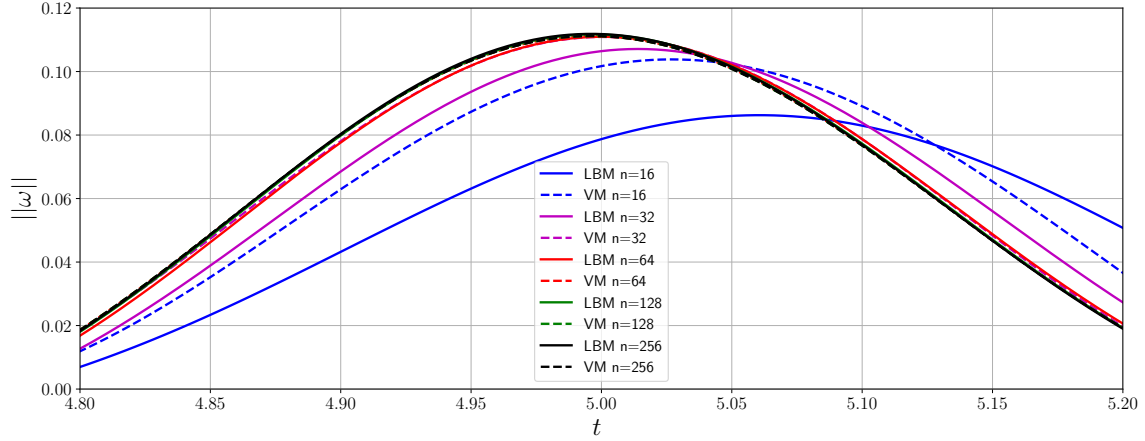


Figure 4: Time evolution of the vorticity norm at the center of the computational domain. Closer view of Figure 3

and by computing the ratio between the last 2 periods and the first 2 periods:

$$G_q = \left( \frac{\int_{9T/2}^{11T/2} \|\mathbf{q}(t)\| dt}{\int_{T/2}^{3T/2} \|\mathbf{q}(t)\| dt} \right)^{1/4T}, \quad (24)$$

where the intervals of time integration  $[\frac{T}{2}, \frac{3T}{2}]$  and  $[\frac{9T}{2}, \frac{11T}{2}]$  are graphically represented by vertical dotted lines in Figure 2.

Figure 6 displays the evolution of  $G_u$  and  $G_\omega$  (velocity and vorticity dissipation respectively) against the numerical wavenumber  $\tilde{k}$ , which is computed by assuming from Figure 1 that the vortex have a global wavelength of  $8r_0$ . As the grid resolutions vary among  $N = 16, 32, 64, 128, 256$  they correspond to numerical wavenumbers respectively equal to:

$$\tilde{k} = k\Delta x = \frac{2\pi}{8r_0} \Delta x = \frac{\pi}{2^{N/5}} = 0.491, 0.245, 0.123, 0.061, 0.031.$$

298 The observed dissipation have similar level for both methods with a slight trend for VM to better  
 299 propagate the low resolved vortex due to its low dispersion brought by the Lagrangian advection  
 300 step. For high resolved vortex, the numerical dissipation produced by both methods tends to  
 301 zero: the total dissipation of the solution tends to the physical viscous dissipation, as can be  
 302 seen on the right hand side of Figure 6 where a comparison of the numerical vorticity dissipation  
 303 with respect to the theoretical dissipation rate of the vorticity mode  $-\nu k^2$  is given.

304 Table 3 gives indicative computational times, obtained respectively with LBM and VM for the  
 305 convected eddy test case. For the coarsest resolutions, namely  $N = 16, 32, 64$ , the data reported  
 306 in the table correspond to the mean of the CPU-times obtained over 10 simulations. Both  
 307 algorithms have been compiled with the standard *gfortran* compiler with similar options. All  
 308 the simulations presented in this table have been performed on the same hardware with only 1  
 309 core (Xeon E7-8860 v4 2.2-3.3 GHz) for all the resolutions. The choice of a unique core allows  
 310 to carry out a comparison detached from any influence of the parallelization level of the two

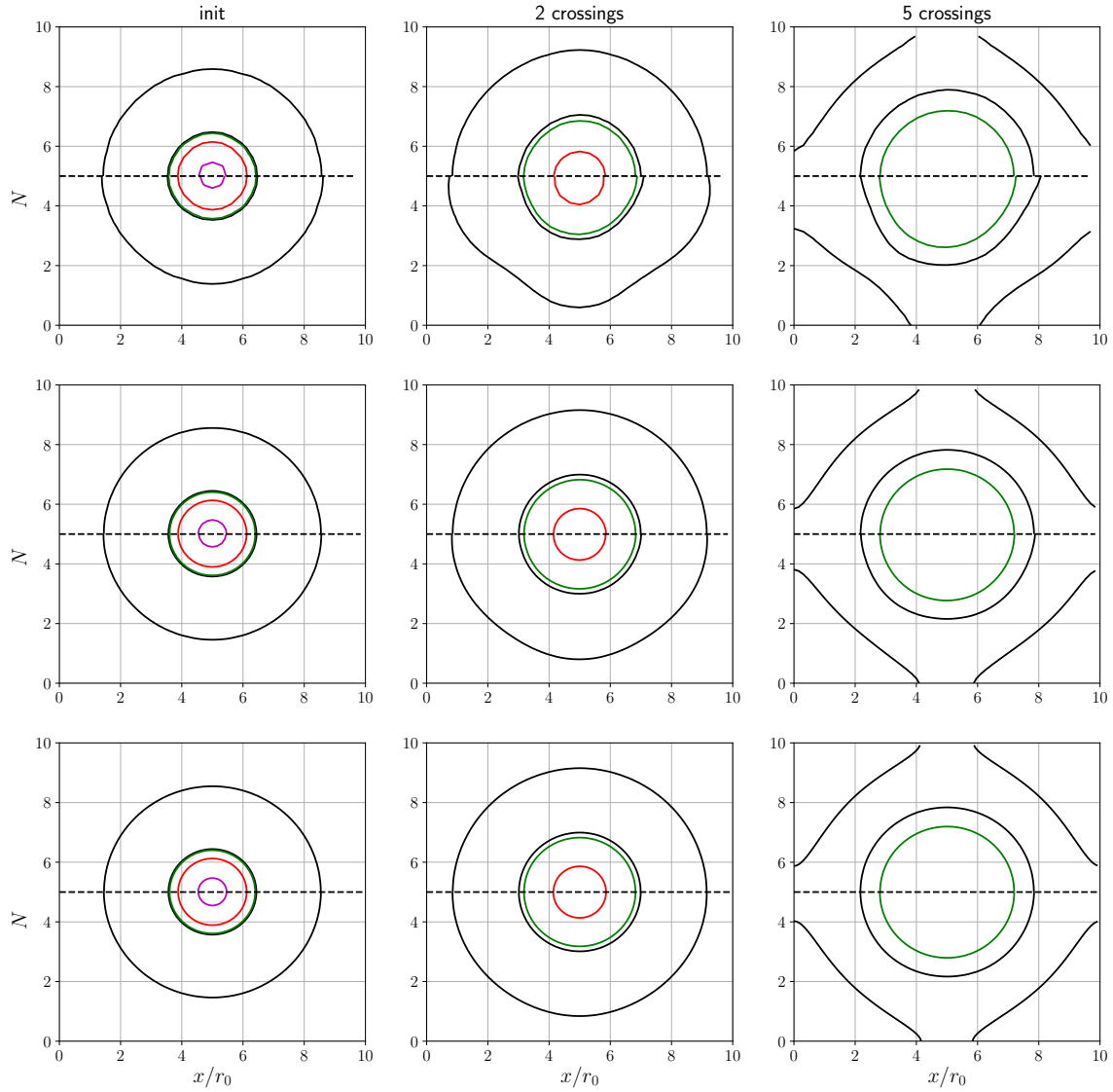


Figure 5: Vorticity isocontours at different resolutions (rows) and different times (columns) (initial time, 2nd domain-crossing and 5th domain-crossing). Each thumbnail shows the face-to-face results for VM (top part) and LBM (bottom part). The isocontours levels are set to  $-0.01$  (black),  $0.01$  (green),  $0.2$  (red) and  $0.8$  (magenta).

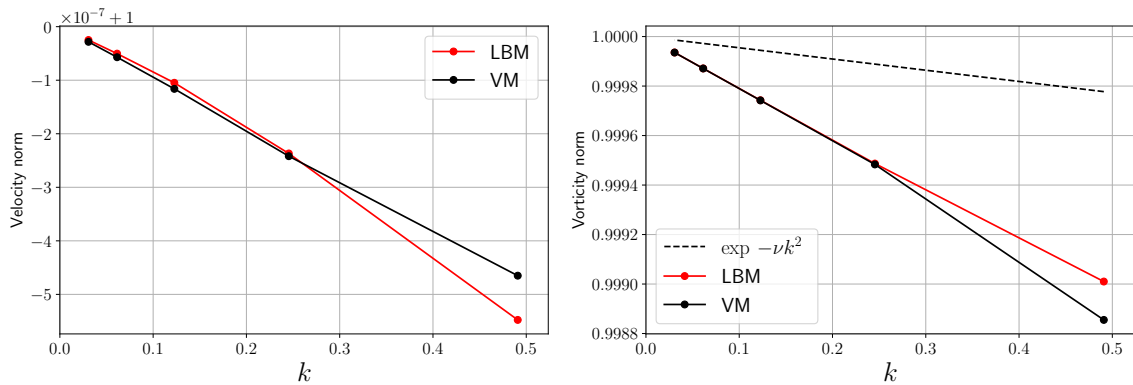


Figure 6: Numerical dissipation of the velocity (left) and vorticity (right) norm, with respect to the numerical wavenumber. The dashed line represents the theoretical dissipation rate of the vorticity mode [67]  $-\nu k^2$ .

311 associated codes (which, one recalls, have been developed independently). In terms of absolute  
 312 comparison between the LBM and VM CPU-times (in seconds), one can conclude from Table 3  
 313 that the present implementation of LBM is faster than the present implementation of VM by a  
 314 factor of 2 approximately for the finest resolutions. This can be explained by the two respective  
 315 algorithms themselves, where the "RHS update" and "Advection" steps contain more substeps  
 316 in VM than in LBM (see Table 2). However, for the reasons explained in section 1.3, these data  
 317 are to handle very cautiously and might be essentially considered as indicative.

| Resol. $N$ | CPU-time <b>LBM</b>          |                      | CPU-time <b>VM</b>            |                       |
|------------|------------------------------|----------------------|-------------------------------|-----------------------|
|            | absolute (sec)               | normalized           | absolute (sec)                | normalized            |
| 16         | 0.276                        | 1                    | 1.80                          | 1                     |
| 32         | 3.12                         | 11 ( $\times$ 11)    | 10.72                         | 6 ( $\times$ 6)       |
| 64         | 53.57                        | 194 ( $\times$ 17.5) | 116.08 ( $\sim$ 2 min)        | 65 ( $\times$ 11)     |
| 128        | 1176.26 ( $\sim$ 20 min)     | 4262 ( $\times$ 22)  | 1921.40 ( $\sim$ 32 min)      | 1070 ( $\times$ 16.5) |
| 256        | 19112.48 ( $\sim$ 5h 20 min) | 69248 ( $\times$ 16) | 36598.16 ( $\sim$ 10h 10 min) | 20378 ( $\times$ 19)  |

Table 3: Comparison of the CPU times required for LBM and VM approaches on the convected eddy test case for the time range  $t^* \in [0, 1]$ . All simulations are performed on a single processor and the CPU times are given in absolute values (in seconds) and normalized according to the CPU-time associated to the  $N = 16$  simulation.

## 318 2.2. Taylor-Green Vortex

319 In order to study the effect of numerical dissipation on a fully 3D turbulent and highly docu-  
 320 mented test-case, the decaying Taylor-Green vortex (TGV) is now considered. It is a fundamental  
 321 benchmark used as prototype for vortex stretching and production of small-scale eddies which  
 322 therefore allows to study the dynamics of transition to turbulence. This test-case has been widely  
 323 used to study the dissipation errors of numerical schemes or the impact of collision operators in  
 324 LBM [68].

For this test-case, the simulations are performed on a  $2\pi$ -periodic cubic domain  $\Omega$  defined as  $0 \leq x, y, z \leq 2\pi$ , with a Reynolds number equal to  $Re = 1600$ . The initialization of the Taylor-

Green vortex is done by setting velocity and pressure variables as follows:

$$\begin{cases} p &= p_\infty + \frac{\rho_\infty U_\infty^2}{16} [\cos(2z) + 2][\cos(2x) + \cos(2y)] \\ u_x &= U_\infty \sin(x) \cos(y) \cos(z) \\ u_y &= -U_\infty \cos(x) \sin(y) \cos(z) \\ u_z &= 0 \end{cases} \quad (25)$$

325 For the LBM simulation, a peculiar attention has to be made for the initialization of the distri-  
326 bution functions when the initial velocity gradients are not negligible [69, 70].

327 In order to work with non-dimensional quantities, all the displayed quantities are normalized by  
328 an arbitrary length scale  $L$  and velocity scale  $U_\infty$ . From this the non dimensional time is defined  
329 by  $t^* = tU_\infty/L$  and the Reynolds number by  $Re = U_\infty L/\nu$ .

### 330 2.2.1. Time step definition

331 For this benchmark, the time steps of each method are set differently by taking advantage of  
332 each algorithm. For VM, the adaptive time step is used whereas the LBM time step is fixed.  
333 Thus, in contrast with the first test-case where both methods were set with the same CFL, this  
334 benchmark will impose different CFL and will highlight the methods for a set of parameter nat-  
335 urally used in the literature.

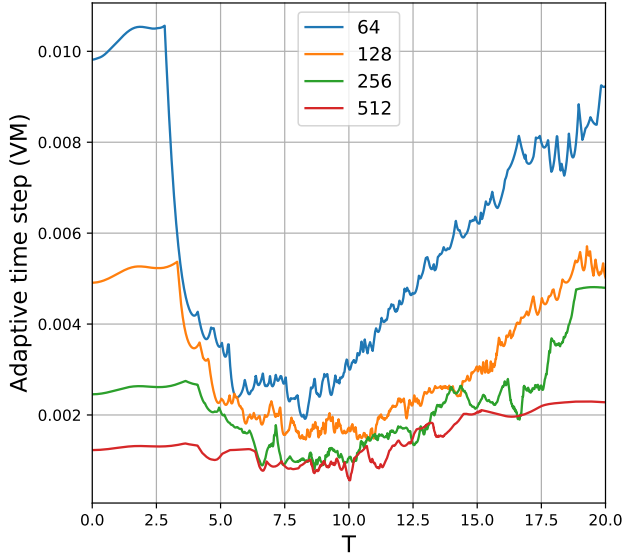
336  
337 All the simulations realized for this test-case are performed in a  $t^* \in [0, 20]$  time range. Different  
338 grid resolutions, denoted  $N^3$ , will be studied, namely  $64^3, 128^3, 256^3$  and  $512^3$ . For LBM com-  
339 putations, the time step is constant and defined by relation (18) (assuming that  $\Delta x = 2\pi/N$ )  
340 and then multiplied by  $U_\infty/L$  to get dimensionless values. This definition gives the following  
341 dimensionless time steps, with respect to the different resolutions :  $\Delta t_{64} \approx 4.8 \cdot 10^{-3}, \Delta t_{128} \approx$   
342  $2.4 \cdot 10^{-3}, \Delta t_{256} \approx 1.2 \cdot 10^{-3}, \Delta t_{512} \approx 6.0 \cdot 10^{-4}$ .

Regarding the VM simulations, the time step is adaptive, based on relation (7), namely  $\Delta t_{\text{LCFL}}^n \leq$   
 $\frac{\text{LCFL}}{\|\nabla \mathbf{u}\|_\infty^n}$  with  $\text{LCFL} < 1$ . More precisely, in these TGV computations, the global adaptive time  
step chosen all along VM simulations is defined by :

$$\Delta t_{\text{adapt}}^n = \min(\Delta t_{\text{CFL}}^n, \Delta t_{\text{LCFL}}^n) = \min\left(\frac{\text{CFL} \cdot \Delta x}{\|\mathbf{u}\|_\infty^n}, \frac{\text{LCFL}}{\|\nabla \mathbf{u}\|_\infty^n}\right) \quad (26)$$

343 where  $n$  denotes the current iteration and where  $\Delta t_{\text{CFL}}^n$  refers to the classical Eulerian stability  
344 condition based on the grid size  $\Delta x$ . In the following TGV simulations, the values of CFL and  
345 LCFL numbers will be respectively set to  $\text{CFL} = 0.1$  and  $\text{LCFL} = 1/32$ . The left handside of  
346 Figure 7 shows the temporal evolution this adaptive time step along VM simulations depending  
347 on the different grid resolutions under study. For each resolution, one can clearly distinguish  
348 between  $t^* = 2.5$  and  $t^* = 5$  the switch from the CFL stability condition to the LCFL one.  
349 The evolution of  $\Delta t_{\text{adapt}}^n$  follows the flow dynamics and shows minimum values in the time range





| Grid resolution | # time steps LBM | # time steps VM |
|-----------------|------------------|-----------------|
| $64^3$          | 4153             | 4411            |
| $128^3$         | 8306             | 7395            |
| $256^3$         | 16612            | 10849           |
| $512^3$         | 33224            | 15324           |

Figure 7: (Left) Temporal evolution of the adaptive time step along VM simulations depending on grid resolution. (Right) Comparison of number of time steps required to achieve a TGV simulation until  $t^* = 20$  between LBM and VM.

350 corresponding to the peak of energy dissipation, at  $t^* \approx 9$  (see next subsection for a clear  
 351 observation of this peak).

352 For purpose of comparison, the table located on the right hand-side of Figure 7 reports the  
 353 number of time steps required respectively in LBM and VM computations to perform a TGV  
 354 simulation until  $t^* = 20$ . In LBM, since  $\Delta t$  is governed by a CFL condition, the number of total  
 355 time steps is successively multiplied by 2 when increasing the grid resolution. In VM, it can be  
 356 noticed that, when  $\Delta t_{\text{adapt}}$  is driven by the LCFL condition, its value at a given resolution is  
 357 not divided by two with respect to the previous coarser resolution (as it is the case when the  
 358 CFL condition governs). This can be explained by the fact that the LCFL condition is based  
 359 on velocity gradients, not on grid step. Thus, the finer is the grid resolution, the better is the  
 360 evaluation of these gradients and higher is the gain in terms of total time steps.

### 361 2.2.2. Time evolution of kinetic energy

362 This subsection is dedicated to the study of the temporal evolution of the kinetic energy  $E =$   
 363  $\frac{1}{2} \int_{\Omega} \|\mathbf{u}\|^2 d\Omega$ , the kinetic energy dissipation rate  $\varepsilon = -\frac{dE}{dt}$  and the enstrophy  $Z = \frac{1}{2} \int_{\Omega} \|\boldsymbol{\omega}\|^2 d\Omega$ .  
 364 Note that the kinetic energy decays proportionally to enstrophy and  $\varepsilon$  and  $Z$  are linked by the  
 365 following relation :  $\varepsilon = -\frac{dE}{dt} = 2\nu Z$ , where  $\nu$  denotes the kinematic viscosity of the fluid.

366 For VM computations, the energy dissipation rate  $\varepsilon$  is reconstructed *a posteriori* using a second  
 367 order time integration scheme ( $\varepsilon = -\frac{(E(t+m\Delta t_{\text{adapt}}) - E(t-m\Delta t_{\text{adapt}}))}{2m\Delta t_{\text{adapt}}}$ ), where  $m$  is chosen to be equal  
 368 to 3 in this study to prevent from spurious oscillations. For LBM calculations, the enstrophy  $Z$   
 369 is computed from the vorticity for which a second order reconstruction is used.

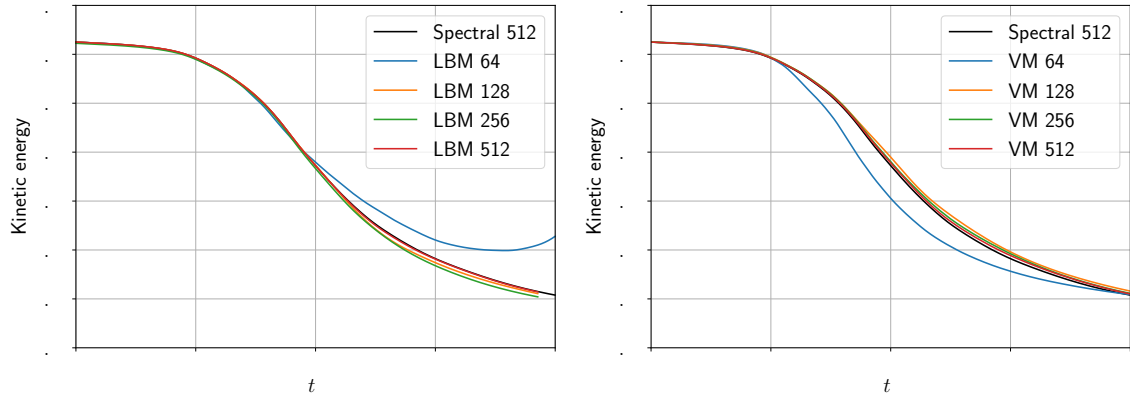


Figure 8: Kinetic energy decay for Taylor-Green vortex benchmark between  $t^* = 0$  and  $t^* = 20$ . (Left) LBM, (Right) VM.

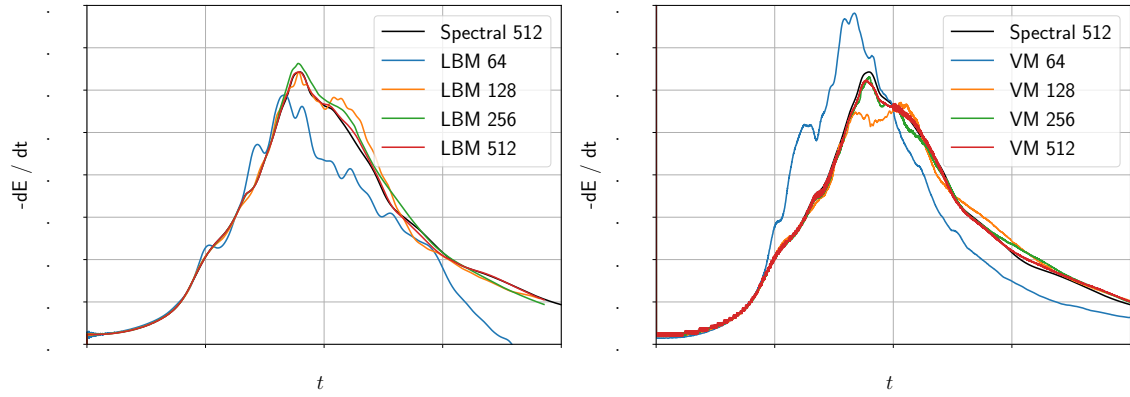


Figure 9: Time evolution of kinetic energy dissipation rate  $\varepsilon = -\frac{dE}{dt}$  for Taylor-Green vortex benchmark between  $t^* = 0$  and  $t^* = 20$ . (Left) LBM, (Right) VM.

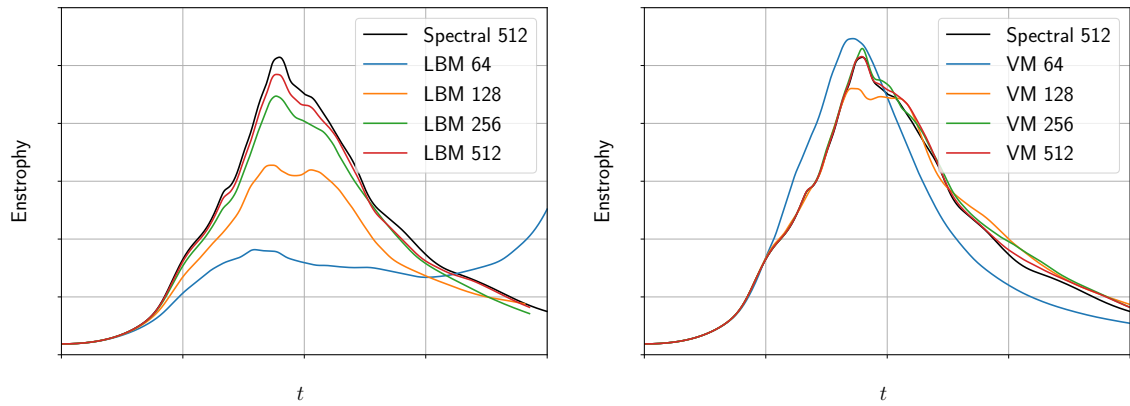


Figure 10: Time evolution of enstrophy  $Z = \frac{1}{2} \int_{\Omega} \|\omega\|^2 d\Omega$  for Taylor-Green vortex benchmark between  $t^* = 0$  and  $t^* = 20$ . (Left) LBM, (Right) VM.

370 Figures 8, 9, 10 respectively show the temporal evolution of  $E$ ,  $\varepsilon$  and  $Z$  for LBM (left) and VM  
 371 (right) for different grid resolutions. The results are compared to the spectral solution at  $512^3$ ,  
 372 taken as the reference solution [71]. As can be seen, both LBM and VM converge towards the  
 373 reference solution, for each physical quantity. In particular, both approaches correctly recover  
 374 the peak of energy dissipation as well as the peak of enstrophy reached at  $t^* \approx 9$  (Figs. 9, 10).  
 375 However, this convergence behaves in a different way : with LBM, the simulation results converge  
 376 from "bottom to top" towards the reference, which illustrates the numerical dissipation brought  
 377 by the Lattice Boltzmann method. From the  $512^3$  grid resolution, the numerical diffusion of  
 378  $E$  and  $\varepsilon$  becomes negligible (cf Figs. 8, 9) and the LBM solution reaches the spectral solution  
 379 with an error of  $10^{-6}$ , as can be seen on the grid convergence curves, Figure 11, which represent  
 380 the  $L^2$ -norm errors of the physical quantities based on the spectral solution on the time range  
 381  $t^* \in [0, 20]$ . As regards enstrophy, which is a second-order-reconstructed quantity in LBM, the  
 382 convergence order is, as expected, close to 2 (cf Figs 10 and 11). However the final enstrophy error  
 383 reached with the finest mesh remains in the order of  $10^{-3}$ . For the coarse resolution, the LBM  
 384 solution is over-dissipated by the grid and the chosen collision model (MRT), despite its ability  
 385 to get stable simulation on coarse grids, still overestimates molecular viscosity when grid step is  
 386 large. A detailed comparison of LBM collision models on the Taylor-Green vortex benchmark  
 387 could be found in [68].

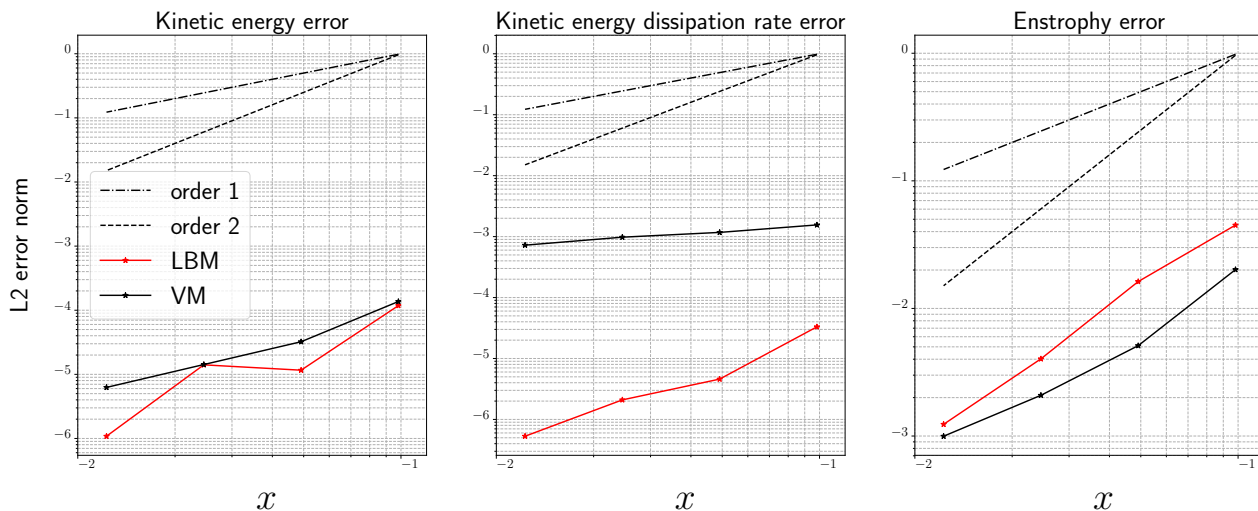


Figure 11: Grid-convergence study for Taylor-Green vortex benchmark between  $t^* = 0$  and  $t^* = 20$ . The  $L^2$ -norm errors of kinetic energy (left), kinetic energy dissipation rate (center) and enstrophy (right) with respect to the spectral solution are plotted against the grid step.

388 Concerning VM, one can observe on Figures 8, 9, 10 a convergence of the solutions from "top to  
 389 bottom" and, more specifically, Figures 9 and 10 reveal that VM tend to slightly over-estimate  
 390 the enstrophy for under-resolved simulations (this phenomenon is shown and proved in [72] and  
 391 can be explained by the antidiffusion mechanisms embedded in the error resulting from the  
 392 reconstruction of particle velocity in Vortex methods). As pointed out in the previous section  
 393 dealing with the convected eddy, VM is a low dissipative method and even for highly under-  
 394 resolved simulations (i.e  $64^3$ ) it manages to provide a rather correct time-evolution of energy

395 decay (Fig. 8) and enstrophy (Fig. 10). At the  $512^3$  resolution, VM reaches the spectral  
 396 solutions with the same ranges of error than LBM, except for the  $\varepsilon$  quantity (cf center of Fig.  
 397 11), which is only reconstructed at the first order in the present remeshed Vortex method.  
 398 Nevertheless, one can globally observe that the VM convergence order is lower than the one of  
 399 LBM, regardless of the quantity studied (cf Figs 11). In particular, the enstrophy convergence  
 400 order achieved with VM (approx 1.43) is slightly lower than LBM (approx 1.76) whereas the  
 401 vorticity  $\omega$ , involved in the enstrophy, represents the primary quantity solved by Vortex methods.  
 402 On one side, as mentioned in section 1.1, the heterogeneous construction of the fractional VM  
 403 algorithm offers a flexible framework to design arbitrarily a semi-Lagrangian numerical method,  
 404 based on previous theoretical works, but on the other hand this heterogeneity makes the *a priori*  
 405 determination of the global order of the method delicate. Numerically, the global order of the  
 406 VM grid-convergence turns out to be a bit less than 2, despite the use of 4<sup>th</sup> order or spectral  
 407 schemes (cf Tab. 2). Some elements like the linear interpolation of the particle velocity in the  
 408 Lagrangian transport or the first order evaluation of the integral quantities  $E$  and  $Z$  can explain  
 409 this behavior.

### 410 2.2.3. Spectral analysis

411 Figure 12 shows turbulent kinetic energy spectra obtained with LBM (left) and VM (right).  
 412 These spectra are plotted at  $t^* = 12$  in order to study the energy cascade throughout the different  
 413 spatial scales at a time when the turbulent flow is developed. Note that the "wavenumber" label  
 414 on the x-axis refers to the mean over the unit sphere of all the wavenumbers  $(k_x, k_y, k_z)$ , that is  
 415 to say to the quantity  $|\mathbf{k}| = \sqrt{(k_x^2 + k_y^2 + k_z^2)}$ . For both methods, a cutoff has been applied to  
 416 the spectra below the cutoff wavenumber corresponding to the smallest resolved scale (vertical  
 417 dotted lines). One can notice that for the coarsest resolution  $64^3$ , LBM slightly overestimates  
 418 the kinetic energy in the resolved scales, while the opposite behavior is observed for VM. This  
 419 confirms the results depicted in Figure 8.

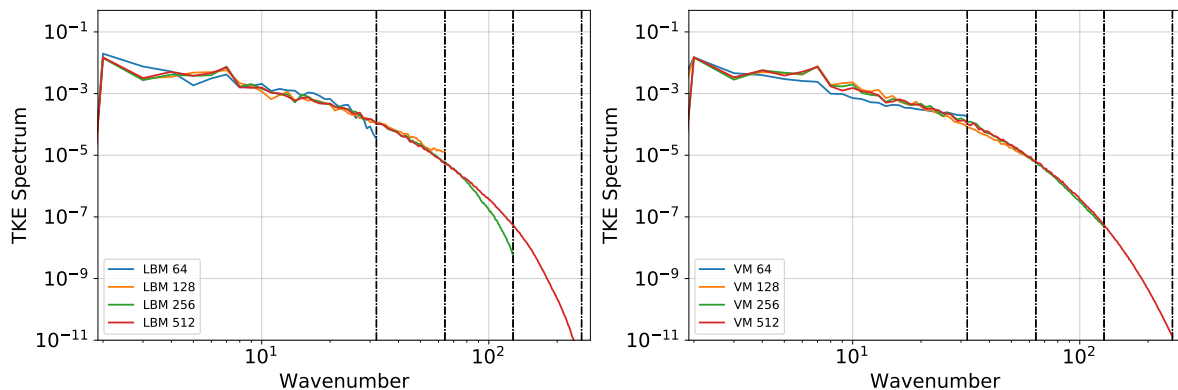


Figure 12: Turbulent kinetic energy spectrum for Taylor-Green vortex benchmark at  $t^* = 12$ . (Left) LBM. (Right) VM. Vertical dotted lines refer to the cutoff wavenumbers associated to the smallest resolved scales.

420 If we now consider the spectra at resolution  $256^3$  and  $512^3$ , the energy cascade in the inertial

421 range seems converged for both method. In the dissipation range, it can be seen that LBM tends  
 422 to dissipate more energy when going towards the cutoff wavenumber, which confirms the remark  
 423 formulated before, stating that VM is globally less dissipative than LBM.

#### 424 2.2.4. Flow structures

425 This last subsection relies on a qualitative comparison between the vortical structures obtained  
 426 in the LBM and VM solutions. Figures 13 and 14 respectively show the vorticity and velocity  
 427 norm of the flow field in the symmetric and periodic half-plane  $x = \pi$ , at  $t^* = 9$  with a  $512^3$   
 428 resolution. As can be seen, at this resolution, the flow structures are significantly comparable  
 429 between LBM and VM.

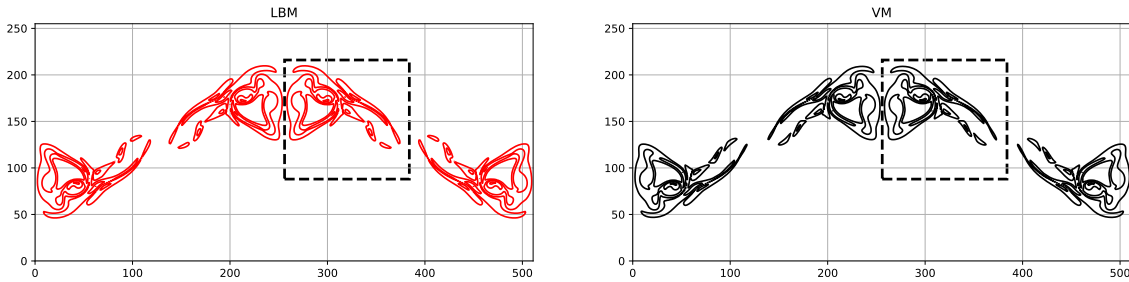


Figure 13: Isocontours of vorticity norm at time  $t^* = 9$  and at levels 1, 5, 10, 20, 30 obtained with a  $512^3$  resolution on the periodic and symmetric half-plane  $x = \pi$ . (Left) LBM. (Right) VM.

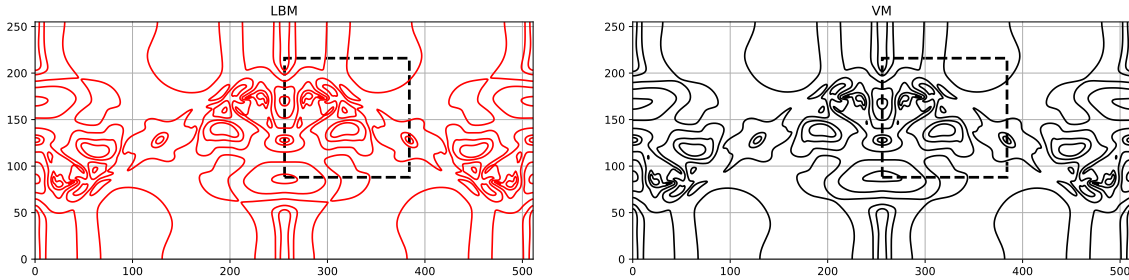


Figure 14: Isocontours of velocity norm at time  $t^* = 9$  and at levels 0.1, 0.2, 0.4, 0.6, 0.8, 1 obtained with a  $512^3$  resolution on the periodic and symmetric half-plane  $x = \pi$ . (Left) LBM. (Right) VM.

430 An enlargement of the main vortical pattern (delimited by the dotted square in Figures 13 and  
 431 14) is proposed in Figure 15, and despite little discrepancies about the vorticity (left) and velocity  
 432 (right) norms, both methods manage to correctly take into account the small scales of the flow.  
 433 In particular it is interesting to look at the vorticity isocontours into more details since they  
 434 bring most of the crucial information of the Taylor-Green flow. Indeed, at  $t^* = 9$  the energy  
 435 dissipation reaches its maximum (cf Fig. 9) and the coherent structures of the flow start to be  
 436 destroyed, leading to the development of the turbulent flow. On Figure 13, the phenomenon  
 437 of rupture of the main vortical structures is clearly observable and very similar for LBM and  
 438 VM. More precisely, on the left hand-side of Figure 15 one can see that both method manage  
 439 to recover the regions of the flow corresponding to vortex tubes (thin elongated structures on

440 the right) which are associated to strong vorticity and small scales, as well as the sheet-like  
 441 structure (large "eye-like" structure on the left) that is associated to strong energy dissipation.  
 442 The few discrepancies existing between the two solutions mainly rely on a little spacial shifting,  
 443 rather than a capacity of catching the tears of the small scale vortex tubes or the contours of  
 444 the sheet-like structure.

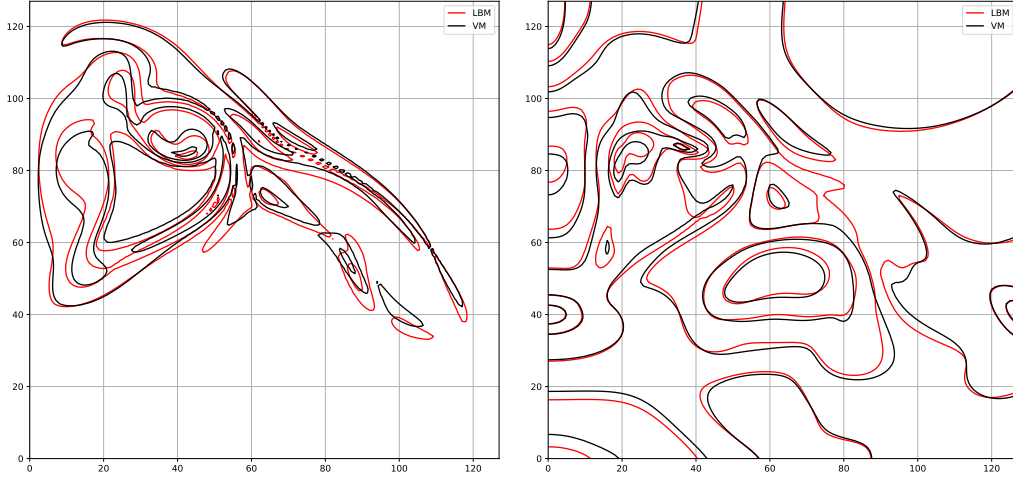


Figure 15: Isocontours at time  $t^* = 9$  with a  $512^3$  resolution on the plane  $x = \pi$ . (Left) Superimposition of isocontours of vorticity norm at levels 1, 5, 10, 20, 30 obtained with LBM (red) and VM (black). (Right) Superimposition of isocontours of velocity norm at levels 0.1, 0.2, 0.4, 0.6, 0.8, 1 obtained with LBM (red) and VM (black).

### 445 3. Flow past a solid cube

446 The last test case proposed in this paper is the flow past a 3D cube fully immersed in the fluid,  
 447 for different regimes. It aims at providing to the present list of benchmarks a significant test  
 448 where the treatment of no-slip boundary conditions is investigated and compared for both LBM  
 449 and VM methods in the proper methodological context where they are usually applied. First  
 450 of all, it has to be noted that, to the authors knowledge, the flow past a 3D cube test-case has  
 451 been subject to rather few number of experimental or numerical studies compared to the case  
 452 of flow past a surface-mounted cube or flow past a sphere. It therefore represents an interesting  
 453 non-usual benchmark for the present study, characterized in particular by the sensitivity of the  
 454 numerical results to the sharp corners of such bluff body. Two different flow regimes will be  
 455 handled in this study to directly compare the effects of wall treatment for both methods. The  
 456 first chosen regime is at  $Re = 290$ , which corresponds to an unsteady and planar symmetric flow  
 457 [73]. The second regime of study is at  $Re = 570$ , where no symmetry is observed in the wake  
 458 and for which the flow becomes fully unsteady [73, 74].

### 459 3.1. Boundary conditions

#### 460 3.1.1. Vortex Method framework

461 The approach used in the present remeshed VM method to handle the no-slip boundary condition  
462 at the solid cube interface is the Brinkman penalization method. The latter, firstly proposed by  
463 [75] and further developed by [76, 77], is part of the immersed boundary methods. It consists in  
464 extending the fluid velocity inside the body and then to penalize it through an extra term in the  
465 Navier-Stokes equations. This penalization term, added as a forcing term, models the no-slip  
466 boundary conditions and is driven by a penalization factor, which can be related to the effective  
467 porosity of the body. Such approach is therefore fully compatible with the use of FFT-based  
468 evaluations for the computation of the velocity field (see eq. (9)), for any type of body geometry.  
469 The Brinkman penalization method has been widely used in the context of semi-Lagrangian  
470 Vortex methods dealing with complex body geometries, because of its efficiency and simplicity  
471 [16, 18, 78, 79, 80]. For the computation of the drag and lift forces, VM simulations use the so  
472 called momentum change approach based on [81] which gives the force acting on the wall surface.  
473 Some other approaches may also be used to compute the aerodynamic forces in the context of  
474 vortex methods with Brinkman penalization [79], where a Poisson equation is solved to evaluate  
475 the pressure field from the velocity. Concerning the output boundary conditions, the present  
476 VM method uses periodic boundary conditions. In order to prescribe the desired uniform flow at  
477 the inlet as well as proper outlet conditions, an absorption region is added at the outlet (cf the  
478 following subsection 3.2). Then a correction of the velocity field has to be performed in order to  
479 recover the desired flux at the inlet and to ensure a non-zero circulation in the computational  
480 domain. We refer the reader to [78] for further details about these aspects.

#### 481 3.1.2. Lattice Boltzmann framework

482 For the lattice Boltzmann simulations, the inflow boundary conditions are set through the equi-  
483 librium distribution function by imposing a uniform streamwise velocity at the inlet and the  
484 outflow boundary conditions imposes a conservation of the non-equilibrium distribution func-  
485 tions at the outlet [82]. A sponge zone is used to increase the viscosity at the outlet and damp  
486 the outgoing structures. The shape of the sponge zone is the same as for VM and is described  
487 in the next subsection. For the computation of forces, the pressure is directly integrated on each  
488 elementary surface and projected in each direction to get the normalized coefficients of Tables 5  
489 and 6. The no-slip condition is imposed with the non-equilibrium bounce-back condition which  
490 corrects the wall output non-equilibrium distributions with their symmetric counterpart from the  
491 wall normal direction [83, 84]. The treatment of no-slip boundary condition with bounce-back is  
492 not the only possibility [85] but could be considered as a standard and efficient way to investigate  
493 no-slip conditions on Cartesian geometries.

### 494 3.2. Numerical setup

495 The study of the flow past a 3D cube is performed for both methods on a uniform Cartesian grid  
496 by imposing a number of  $n$  grid points along the cube length  $D$ . The size of the computational  
497 domain is defined in terms of the cube length and set to  $[-L_u, L_d] \times [-H/2, H/2] \times [-H/2, H/2]$ .



498 The associated blockage ratio, BR, is defined as the ratio of the cube length and the domain  
499 cross-section, i.e.  $D/H^2$ . The center of the cube is located at the origin  $(x, y, z) = (0, 0, 0)$  of the  
500 domain. The reference values  $U_\infty$  and  $D$  are set to unity such that the grid step is defined by  
501  $h = D/n$ . The different grid parameters considered in the cube simulations are summarized in  
502 Table 4, depending on the Reynolds number, and a schematic representation of the computation  
503 domain is given in Figure 16.

|            | $n$ | $N_x$ | $N_y$ | $N_z$ | $h$    | Domain   | BR    |
|------------|-----|-------|-------|-------|--------|--|-------|
| $Re = 290$ |     |       |       |       |        |  |       |
|            | 25  | 320   | 128   | 128   | 0.04   | $[-2, 10.8] \times [-2.56, 2.56] \times [-2.56, 2.56]$ | 3.81% |
|            | 50  | 640   | 256   | 256   | 0.02   | $[-2, 10.8] \times [-2.56, 2.56] \times [-2.56, 2.56]$ | 3.81% |
| $Re = 570$ |     |       |       |       |        |  |       |
|            | 80  | 1024  | 512   | 512   | 0.0125 | $[-2, 10.8] \times [-3.2, 3.2] \times [-3.2, 3.2]$     | 2.44% |

Table 4: Grid parameters used for the cube simulation at  $Re = 290$  and  $Re = 570$  for both LBM and VM.

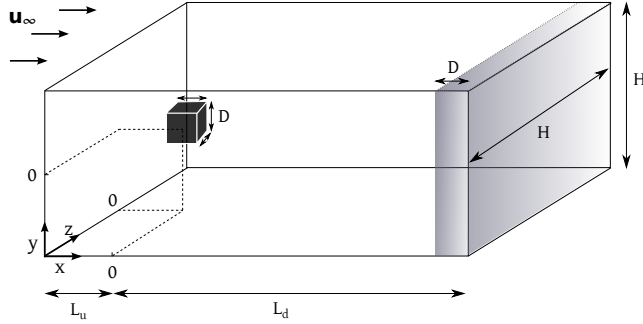


Figure 16: Computational domain, including the outlet sponge zone, for flow past a 3D cube.

For both LBM and VM methods, a sponge zone is added at the outlet of the domain  $\mathcal{D}$  to prescribe the absorbing boundary condition. The absorption is performed according to the following one-dimensional smoothing function  $f$  defined in the flow direction (i.e.  $x$ -direction):

$$f(x) = \begin{cases} 1 & \text{if } x < x_b \\ \frac{\tanh(\alpha(x-x_c)) - \tanh(\alpha(x_e-x_c))}{\tanh(\alpha(x_b-x_c)) - \tanh(\alpha(x_e-x_c))} & \text{if } x_b \leq x \leq x_e \\ 0 & \text{if } x > x_e \end{cases} \quad (27)$$

504 where  $x_b$ ,  $x_c$  and  $x_e$  respectively refer to the beginning, the center and the end of the absorption  
505 band at the outlet. The parameter  $\alpha$  allows to adjust the steepness of the absorption function  
506  $f$ . In both LBM and VM approaches, one sets  $\alpha = 10$ ,  $x_b = L_d - D$  and  $x_e = L_d$  (width equal  
507 to  $1D$ ), which accounts for less than 8% of the total size, and thus of the total computational  
508 cost. A uniform velocity field  $\mathbf{u}_\infty = (u_{x\infty}, u_{y\infty}, u_{z\infty}) = (U_\infty, 0, 0) = (1, 0, 0)$  is set at the inlet of  
509 the domain. In order to trigger the instability in a similar way for both methods, a perturbation  
510 is applied during the simulation between  $t^* = 3$  and  $t^* = 4$  on the  $y$  component of the velocity,  
511 defined by  $u_{y\infty} = 0.1 \sin(\pi(T - 3))$ . For LBM, the time-step value is defined by (18) imposing  
512 a CFL number based on  $U_\infty$ , equal to 0.1, and for VM, the time step is adaptive, according to  
513 relation (26), taking  $\text{CFL} = 0.5$  and  $\text{LCFL} = 0.125$ .

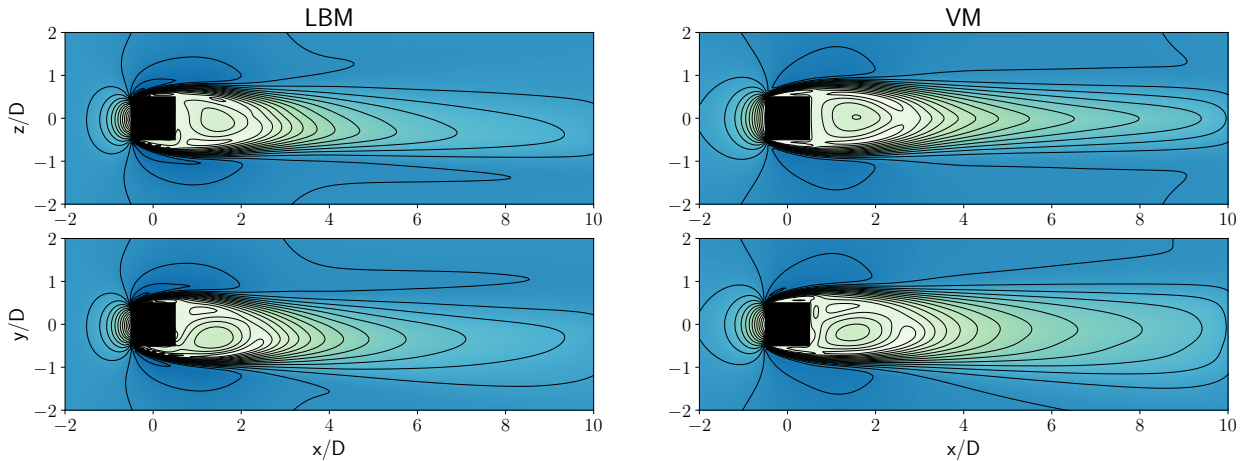


514 Two Reynolds numbers are investigated here,  $Re = 290$  and  $Re = 570$ . One notices that the aim  
515 of this section is not to carry out an exhaustive study of the physics related to this type of flows,  
516 but rather to compare the behavior of two numerical methods based on the same geometrical  
517 setup with boundary conditions usually applied in their proper computational context.

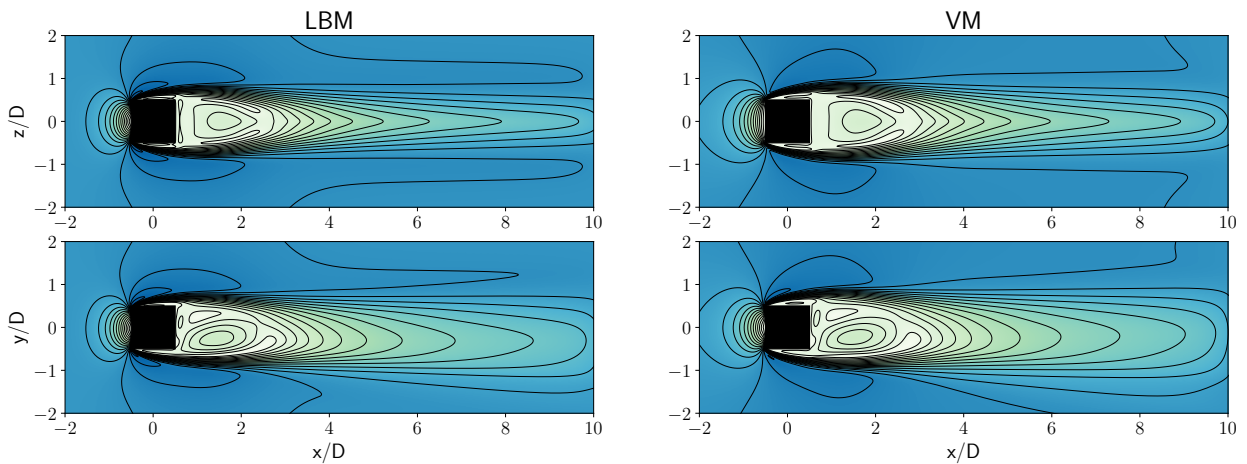
### 518 3.3. Results and discussion

519 Let us first investigate the results for the flow around a cube at  $Re = 290$ . As reported in Table 4,  
520 at this regime the simulations are performed for both methods at 2 grid levels, namely with  $n = 25$   
521 and  $n = 50$ . The simulations are realized on a total characteristic time of  $t^* = tU_\infty/D = 150$ .  
522 The mean quantities are averaged during the period from  $t^* = 50$  to the end of the simulation.  
523 Figure 17 shows the norm of the mean velocity components. The solutions at the two grid levels  
524 are represented in the two orthogonal planes in the streamwise direction of the flow, namely  
525 the XZ and XY planes. These results on mean flows are complemented by Figure 18, giving the  
526 associated streamwise velocity profiles along  $x$  and  $y$  direction. The first observation that one can  
527 make from these two figures, is that both LBM and VM methods reach with  $n = 50$  the planar  
528 symmetric flow in XZ plane, as expected and reported in literature [73, 74]; indeed, on Figure  
529 17b the mean flows in XZ plane clearly show a symmetry with respect to the centerline of the  
530 wake and the non-planar symmetric wakes in XY plane exhibit comparable isocontours and more  
531 specifically a qualitatively similar ex-centred recirculation zone downstream. On Figure 18-right,  
532 the  $z$ -profiles of both methods for  $n = 50$  (solid lines) are also distinctly symmetric. What is also  
533 interesting to notice, is the way the two methods converge to the planar symmetric flow state:  
534 as also highlighted in the two previous test cases of this paper, VM achieves better results at  
535 coarser grid resolution than LBM which fails at  $n = 25$  in computing a planar symmetric flow  
536 for the same grid configuration (see XZ planes on Fig. 17a and the dotted curves on Fig. 18).

537 If we now focus more precisely on the mean velocity profiles in Figures 18, one can observe a  
538 velocity difference on Figure 18-left where the VM inlet velocity appears to be slightly lower than  
539 the expected far-field velocity, correctly restored by LBM. As a consequence, the levels of Figure  
540 17 are noticeably different in the inlet region for the two methods. These discrepancies may be  
541 explained by the velocity correction performed in VM in order to account for non-periodic flow  
542 in the domain. This correction prescribes the uniform inlet flow rate with an error compared to  
543 the theoretical one based on the desired inlet velocity field ( $\mathbf{u}_\infty = (1, 0, 0)$ ). However, despite  
544 these differences close to the domain walls, it is interesting to see that the solution close to the  
545 solid boundaries is comparable for LBM (with bounce-back conditions) and VM (with Brinkman  
546 penalization method), which highlights the ability of both methods to treat correctly no-slip  
547 boundary conditions. Among the differences in the obstacle region, one can first remark that  
548 VM results exhibit a slightly thicker recirculation zone induced by a larger detached flow region  
549 near the wall. This is more visible on Figure 18-right where the VM velocity profile is larger  
550 than LBM in the  $z$ -direction. Moreover, one can concentrate on the  $x/D = [-0.5, 0.5]$  and  
551  $z/D = [-0.5, 0.5]$  regions in Figure 18, corresponding to the solid cube. At the extremities of  
552 these regions, that is to say at the cube surface, the mean velocity profiles of LBM indicate a 0  
553 value which corresponds to the direct prescription of no-slip boundary conditions in the bounce-  
554 back approach. On the other hand, the profiles obtained with VM indicate that the velocity does



(a)  $n = 25$



(b)  $n = 50$

Figure 17: Flow past a cube at  $Re = 290$ . Norm of the mean velocity components ( $\sqrt{\overline{u_x^2} + \overline{u_y^2} + \overline{u_z^2}}$ ) in  $XZ$  (top) and  $XY$  (bottom) planes for LBM (left) and VM (right). Levels correspond to 20 equispaced values between 0 and 1.4 included.

555 not completely vanish inside the solid cube and at its surface. These non-zero values correspond  
 556 to the Brinkman penalization model adopted in the present VM method, which consists, at each  
 557 time step, in allowing the flow to enter the solid obstacle and then to penalize it by considering  
 558 it as an extremely low permeable region according to a penalization coefficient, denoted  $\lambda$ . The  
 559  $\lambda$ -convergence of the Brinkman penalization to real no-slip boundary conditions ( $\mathbf{u} = 0$ ), is of  
 560 order 1 [19]. The ability of both methods to correctly handle the boundary conditions, and  
 561 thus the flow physics, is also confirmed by Figures 19 where are depicted the norm of the mean  
 562 velocity component for flow past a cube at  $Re = 570$ . As reported in literature [74], the flow at  
 563 such regime is unsteady and the wake does not show any symmetry, which is the result observed  
 564 on Figures 19 and 20.

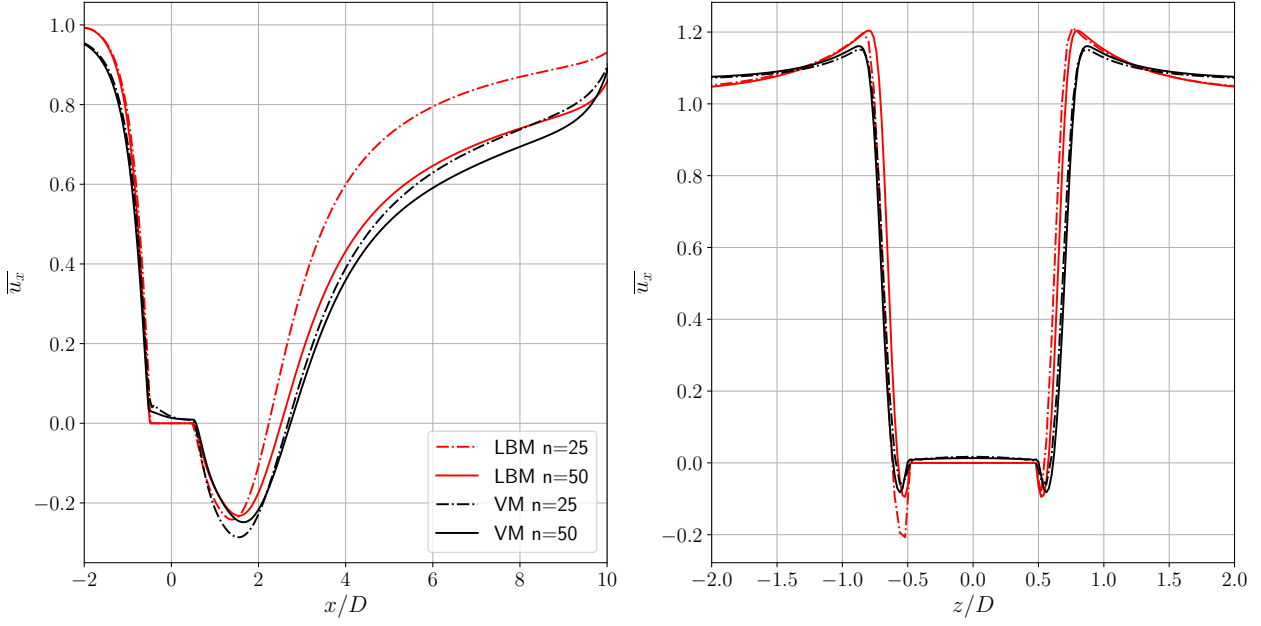


Figure 18: Average streamwise velocity profiles for flow past a cube at  $Re = 290$ . (Left) Along streamwise direction at  $y = 0$  and  $z = 0$ . (Right) Along spanwise direction at  $x = 0$  and  $y = 0$ .

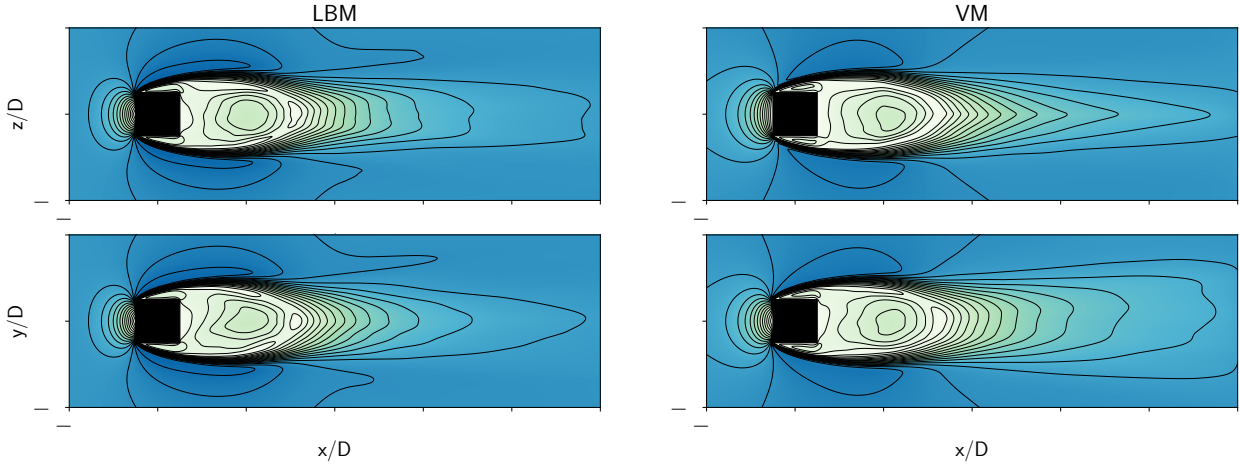


Figure 19: Flow past a cube at  $Re = 570$  with  $n = 80$ . Norm of the mean velocity components ( $\sqrt{u_x^2 + u_y^2 + u_z^2}$ )  $XZ$  (top) and  $XY$  (bottom) planes for LBM (left) and VM (right) (same isocontour levels as Fig. 17).

565 To complement the flow analysis, the two methods are compared in terms of instantaneous  
566 vorticity fields in Figure 21. This figure shows the close-up view of the  $\omega_z$  isocontours for three  
567 different resolutions at  $Re = 570$  in the  $XY$  plane near the solid walls, at  $t^* = 120$ . The interest  
568 of such view is to focus the comparison on the boundary layer region where the flow is laminar,  
569 rather than the wake region which is turbulent and whose analysis at a given time  $t^*$  strongly  
570 depends on the perturbation trigger. One can observe on this figure that the boundary layer  
571 thickness as well as the region of detachment points, located around downstream corners, are

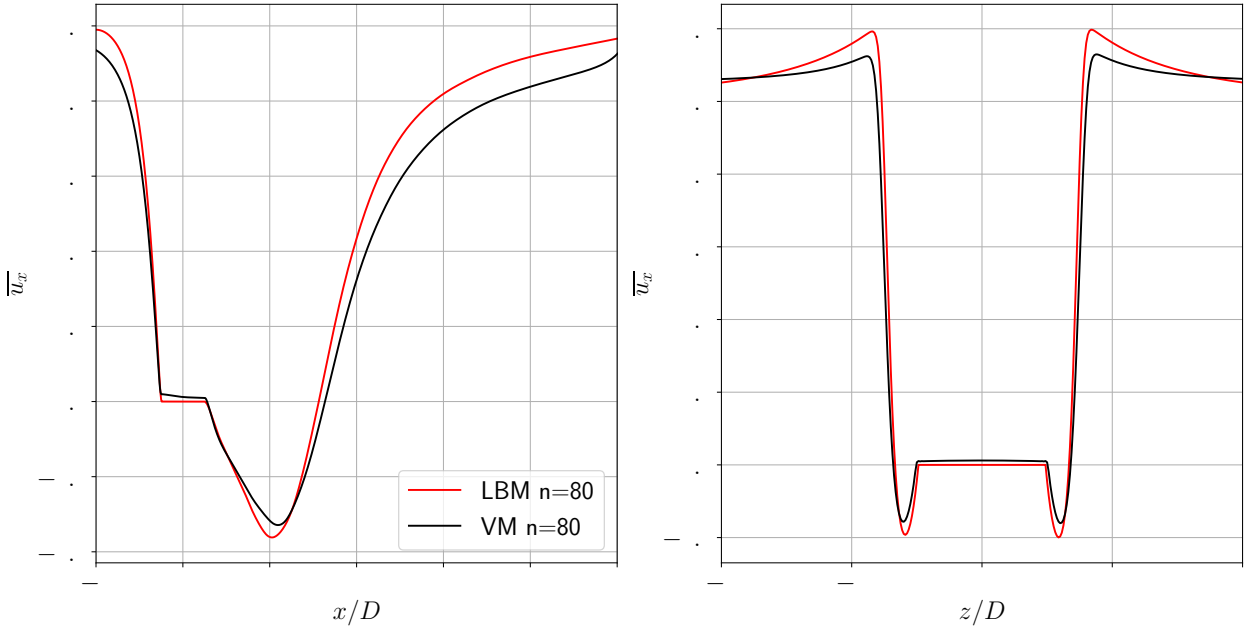


Figure 20: Average streamwise velocity profiles for flow past a cube at  $Re = 570$ . (Left) Along streamwise direction at  $y = 0$  and  $z = 0$ . (Right) Along spanwise direction at  $x = 0$  and  $y = 0$ .

572 very similar between LBM and VM. The main discrepancy occurs at the upstream cube corners,  
 573 where the different boundary conditions adopted by the two methods induce different levels of  
 574 spurious vorticity at these sharp edges. However, the spurious solution in this region turns out  
 575 to be attenuated for both methods when refining the mesh; with  $n = 80$  the thickness and shape  
 576 of the upstream boundary layer are very comparable.

577 Regarding the evaluation of flow characteristics, Tables 5 and 6 report the mean drag, lift and  
 578 side-lift coefficients ( $\bar{c}_D$ ,  $\bar{c}_L$ ,  $\bar{c}_S$ ), the recirculation length ( $l_r$ ) and the Strouhal number ( $St =$   
 579  $fD/U_\infty$ ) obtained at  $Re = 290$  and  $Re = 570$  by LBM and VM as well as those of selected  
 580 references in literature. Concerning the recirculation length, it is defined as the axial distance,  
 581 along the centerline of the wake, between the center of the cube and the point where the mean  
 582 streamwise component of the velocity is zero. First of all, it has to be noted that the cube  
 583 benchmark is not as widely studied in literature as the sphere benchmark, which explains the  
 584 rather few quantity of reference works about such flow. In terms of flow physics, and as explained  
 585 in [74], it is important to mention that the values of  $\bar{c}_D$  for sphere and cube differ as the Reynolds  
 586 number increases: once the Reynolds number has reached the unsteady and planar-symmetric  
 587 regime (ie  $Re \gtrsim 276$ ), the  $\bar{c}_D$  for cube increases with the Reynolds number, contrary to the one  
 588 of the sphere. One can see in Table 5 ( $Re = 290$ ) and Table 6 ( $Re = 570$ ) that this statement  
 589 is verified both by LBM and VM. In terms of comparison, in Table 5, the  $\bar{c}_D$  results of LBM  
 590 and VM are in good accordance with the evaluations of Haider & Levenspiel [86]. On the other  
 591 hand, the results of Saha [73] and Khan *et al.* [74] predict a lower drag coefficient. Concerning  
 592 the Strouhal number at  $Re = 290$ , the LBM and VM results are rather close to the experimental  
 593 result of Klotz *et al.* [87], standing around 0.12, whereas the values reported by Saha and Khan

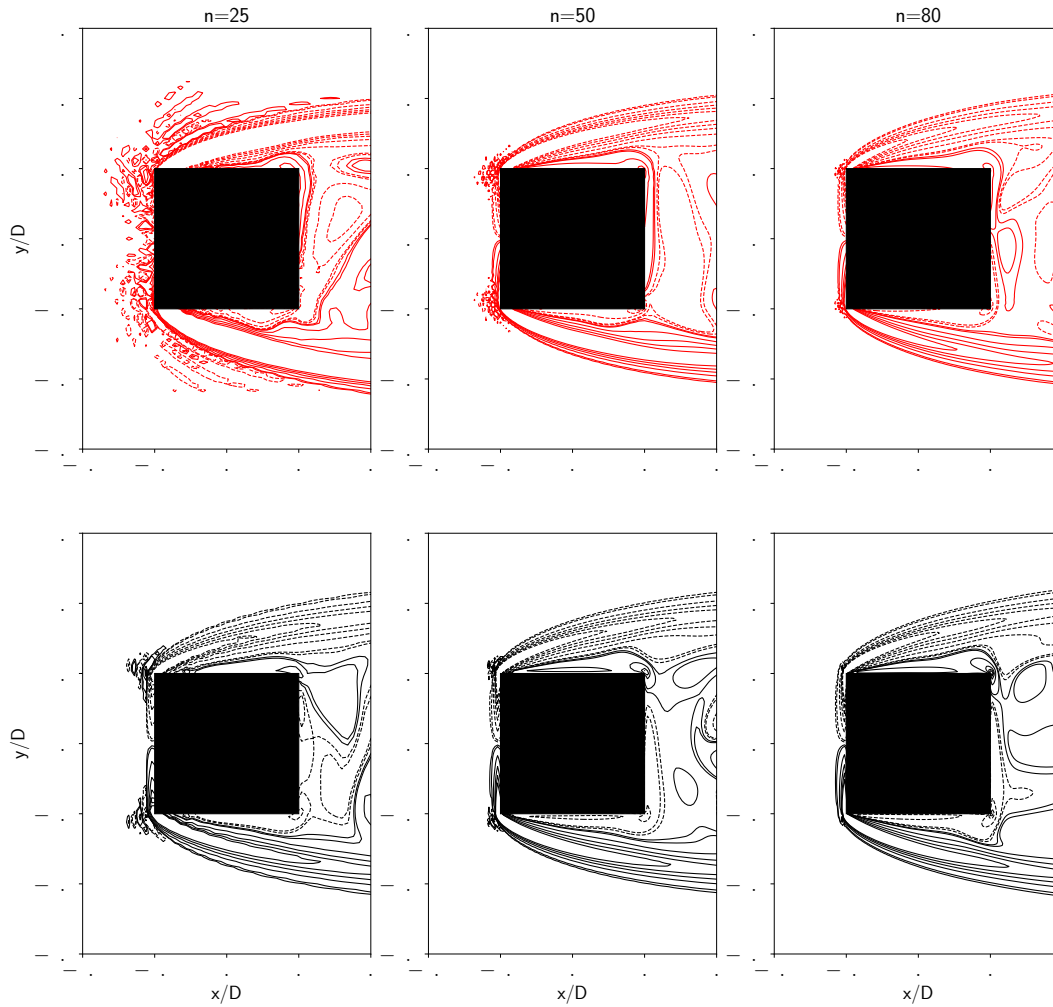


Figure 21:  $\omega_z$  vorticity isocontours for flow past a cube at  $Re = 570$  at  $t^* = 120$ . Levels correspond to 10 equispaced values between -10 and 10 with additional contours at  $\pm 0.5$  and  $\pm 0.25$ , where dashed lines represent negative values. Top(red) LBM and Bottom(Black) VM.

594 *et al.* are lower than 0.1. These differences can be explain by the different numerical setup used  
 595 in the studies with respectively 30 and 20 points along the cube for Saha and Khan *et al.* and  
 596 on the other hand a different blockage ratio of the computational domain; indeed, the present  
 597 BR for simulations at  $Re = 290$  is equal to 3.81% against 0.44% in Khan *et al.* simulations and  
 598 0.51% for Saha. The present BR is closer to the one of Klotz *et al.* (1.44%) which may explain  
 599 the closer results in terms of Strouhal number.

600 It has also to be noted that both LBM and VM methods recover a quasi-zero  $\bar{c}_S$  value at  
 601  $Re = 290$ , which is consistent with the fact that the wake is symmetric in the XZ plane at such  
 602 regime. The sign of the lateral and side lift coefficients has been removed due to the arbitrary  
 603 asymmetry direction chosen by the flow. Indeed, the asymmetry balance can change due to  
 604 infinitesimal computing artefacts without altering the flow behavior and topology. Finally one  
 605 can note that the recirculation length is slightly lower for LBM results. Indeed, the profiles of

606 Figure 18-left show that the LBM mean streamwise velocity in the recirculation area starts to  
607 increase earlier than in the VM results. As mentioned previously, this could be an effect of the  
608 prescribed inflow/outflow boundary conditions for the two methods.

|                          | $\bar{c}_D$ | $\bar{c}_L$ | $\bar{c}_S$          | $l_r$ | $St$                 |
|--------------------------|-------------|-------------|----------------------|-------|----------------------|
| Saha [73]                | 0.783       | 0.064       | 0.0                  | -     | 0.094                |
| Klotz <i>et al.</i> [87] | -           | -           | -                    | 2.63  | 0.128 ( $Re = 292$ ) |
| Khan <i>et al.</i> [74]  | 0.83        | 0.0053      | 0.01646              | 2.50  | 0.098 ( $Re = 300$ ) |
| Haider & Levenspiel [86] | 1.08        | -           | -                    | -     | -                    |
| Present LBM $n = 25$     | 1.093       | 0.136       | 0.039                | 2.20  | 0.120                |
| $n = 50$                 | 0.900       | 0.073       | $4.31 \cdot 10^{-4}$ | 2.50  | 0.120                |
| Present VM $n = 25$      | 0.985       | 0.066       | 0.0041               | 2.64  | 0.120                |
| $n = 50$                 | 1.003       | 0.088       | $8.14 \cdot 10^{-5}$ | 2.72  | 0.120                |

Table 5: Comparison of mean force coefficients, mean recirculation length and Strouhal number for flow past a cube at  $Re = 290$ .

|                          | $\bar{c}_D$ | $\bar{c}_L$ | $\bar{c}_S$ | $l_r$ |
|--------------------------|-------------|-------------|-------------|-------|
| Khan <i>et al.</i> [74]  | 0.91        | 0.0576      | 0.103       | -     |
| Haider & Levenspiel [86] | 1.14        | -           | -           | -     |
| Present LBM ( $n = 80$ ) | 1.121       | 0.005       | 0.011       | 3.13  |
| Present VM ( $n = 80$ )  | 1.014       | 0.003       | 0.013       | 3.26  |

Table 6: Comparison of mean force coefficients, mean recirculation length for flow past a cube at  $Re = 570$ .

## 609 4. Conclusion

610 In this work an algorithmic and numerical comparative study of a Lattice Boltzmann Method  
611 (LBM) and a remeshed Vortex method (VM) was presented in the context of three dimensional  
612 incompressible flows. Both approaches belong to families of methods where the flow is not con-  
613 sidered and discretized in a macroscopic way and where the notion of particles is a common  
614 aspect. In Lattice Boltzmann Methods, the local algorithms and low stencil schemes (lattice)  
615 contribute to their efficiency and allow one to easily implement and parallelize them. Regarding  
616 semi-Lagrangian (remeshed) Vortex methods, they couple optimally Lagrangian and Eulerian  
617 schemes in a fractional step algorithm, which contributes to their flexibility and specificity. In  
618 particular, the Lagrangian treatment of the advection term enables the use of an adaptive  $\Delta t$ ,  
619 thus reducing the total number of time steps within a whole simulation.

620 The two methods were compared with respect to each others and validated with other experi-  
621 mental/numerical results in literature for three reference test cases: the advection of a simple  
622 vortex, the Taylor Green vortex and the flow around a cube in a free domain. The first ob-  
623 servation for the first two benchmarks was the low dissipative and dispersive behaviour of the  
624 present remeshed Vortex method, especially for coarse grids, which offers better results for low  
625 resolutions. The second main observation relies on the fact that the present LBM offers a better

626 accuracy at fine grid resolutions and a higher order of convergence, which also aligns with the  
627 conclusions already made in the literature as previously described.

628 For the cube test case, which is a stiff numerical problem with sharp edges and singularities,  
629 both LBM and VM were used with their own boundary conditions in order to illustrate a typical  
630 use of both algorithms in the context of a more complex and applied benchmark. Once again,  
631 the ability of VM to better compute the expected flow behavior on coarse grids was confirmed.  
632 For higher resolved grids the results of both methods show a good qualitative agreement, the  
633 quantitative discrepancies being mainly due to the different treatment of inlet/outlet and no-slip  
634 boundary conditions within the two methods.

635 All the results presented in this study should be interpreted in the specific context of the chosen  
636 models, which have been mostly tested and compared in terms of global and integral quanti-  
637 ties. Even if some improved versions of these models exist in literature, a deeper analysis of  
638 local behaviors should increase the understanding of each item of the two presented approaches.  
639 Furthermore, in order to fully take advantage of the intrinsic performances of each method, a  
640 hybrid algorithmic implementation should be considered as a target for future developments in  
641 the framework of this family of numerical methods.

## 642 **Acknowledgement**

643 Part of this work was performed using HPC resources from GENCI-CINES (Grant 2019-A0072A10636).  
644 The authors would like to thanks M. Rafik Abdesselam for providing them the JupyterHUB-  
645 Cnam server access for efficient and shared post-processing.

## 646 **References**

- 647 [1] T. Douillet-Grellier, S. Leclaire, D. Vidal, F. Bertrand, F. De Vuyst, Comparison of mul-  
648 tiphase SPH and LBM approaches for the simulation of intermittent flows, *Computational*  
649 *Particle Mechanics* 6 (2019) 695–720.
- 650 [2] W. Prager, Die Druckverteilung an Korpern in ebener Potentialstromung, *Physikalische*  
651 *Zeitschrift* 29 (1928) 865–869.
- 652 [3] L. Rosenhead, The Formation of vortices from a surface of discontinuity, *Proc. R. Soc.*  
653 *London Ser. A* 134(823) (1931) 170–192.
- 654 [4] A. J. Chorin, Numerical study of slightly viscous flow, *J. Fluid Mech.* 57 (1973) 785–796.
- 655 [5] G.-H. Cottet, S. Mas-Gallic, A particle method to solve the Navier-Stokes system, *Num.*  
656 *Math.* 57 (1990) 1–23.
- 657 [6] A. J. Chorin, Vortex sheet approximation of boundary layers, *J. Comput. Phys.* 27 (1978)  
658 428–442.

- 659 [7] Y. M. Marzouk, A. F. Ghoniem, K-means clustering for optimal partitioning and dynamic  
660 load balancing of parallel hierarchical N-body simulations, *J. Comput. Phys.* 207(2) (2005)  
661 493–528.
- 662 [8] Q. Hu, N. Gumerov, R. Yokota, R. Barba, L.A. Duraiswami, Scalable fast multipole methods  
663 for vortex element methods, in: *IEEE Explore*, 1408–1409, 2012.
- 664 [9] R. Yokota, L. A. Barba, N. T., K. Yasuoka, Petascale turbulence simulation using a highly  
665 parallel fast multipole method on GPUs, *Comput. Phys. Commun* 184(3) (2013) 445–455.
- 666 [10] E. Rossi, A. Colagrossi, D. Durante, G. Graziani, Simulating 2D viscous flow around geome-  
667 tries with vertices through the Diffused Vortex Hydrodynamics method, *Comput Methods*  
668 *Appl. Mech. Eng.* 302 (2016) 147–169.
- 669 [11] O. Giannopoulou, A. Colagrossi, A. Di Mascio, C. Mascia, Chorins approaches revisited:  
670 Vortex Particle Method vs Finite Volume Method, *Eng. Anal. Bound. Elem.* 106 (2019)  
671 371–388.
- 672 [12] L. Barba, A. Leonard, C. Allen, Advances in viscous vortex methods meshless spatial  
673 adaption based on radial basis function interpolation, *Int. J. Numer. Methods Fluids* 47(5)  
674 (2005) 387–421.
- 675 [13] E. Rossi, A. Colagrossi, G. Graziani, Numerical simulation of 2D-vorticity dynamics using  
676 Particle Methods, *Comput. Math. with Appl.* 69 (2015) 1484–1503.
- 677 [14] S. Huberson, A. Jollès, Correction de l’erreur de projection dans les méthodes partic-  
678 ules/maillage, *La recherche aérospatiale* 4 (1990) 1–6.
- 679 [15] P. Koumoutsakos, A. Leonard, High-resolution simulations of the flow around an impulsively  
680 started cylinder using Vortex methods, *J. Fluid Mech.* 296 (1995) 1–38.
- 681 [16] M. Coquerelle, G.-H. Cottet, A Vortex level-set method for the two-way coupling of an  
682 incompressible fluid with colliding rigid bodies, *J. Comput. Phys.* 227 (2008) 9121–9137.
- 683 [17] M. Gazzola, P. Chatelain, W. M. Van Rees, P. Koumoutsakos, Simulations of single and  
684 multiple swimmers with non-divergence free deforming geometries, *J. Comput. Phys.* 230  
685 (2011) 7093–7114.
- 686 [18] M. Gazzola, C. Mimeau, A. Tchieu, P. Koumoutsakos, Flow mediated interactions between  
687 two cylinders at finite Re numbers, *Phys. Fluids* 24 (4), doi:10.1063/1.4704195.
- 688 [19] C. Mimeau, F. Gallizio, G.-H. Cottet, I. Mortazavi, Vortex penalization method for bluff  
689 body flows, *Int. J. Numer. Meth. Fluids* doi: 10.1002/flid.4038.
- 690 [20] W. M. Van Rees, M. Gazzola, P. Koumoutsakos, Optimal shapes for anguilliform swimmers  
691 at intermediate Reynolds numbers, *J. Fluid Mech.* 722 (2013) R31–R312.



- 692 [21] C. Mimeau, I. Mortazavi, G.-H. Cottet, Passive control of the flow around a  
693 hemisphere using porous media, *Eur. J. Mech - B/Fluids* 65 (2017) 213–226, doi:  
694 10.1016/j.euromechflu.2017.03.002.
- 695 [22] P. Chatelain, M. Duponcheel, D.-G. Caprace, Y. Marichal, G. Winckelmans, Vortex Particle-  
696 Mesh simulations of vertical axis wind turbine flows: from the airfoil performance to the  
697 very far wake, *Wind Energ. Sci.* 2 (2017) 317–328.
- 698 [23] M. Gazzola, B. Hejazialhosseini, P. Koumoutsakos, Reinforcement learning and wavelet  
699 adapted Vortex methods for simulations of self-propelled swimmers, *SIAM J. Sci. Comput*  
700 36 - 3 (2014) B622–B639.
- 701 [24] Y.-H. Qian, D. d’Humières, P. Lallemand, Lattice BGK models for Navier-Stokes equation,  
702 *Europhys. Lett.* 17 (1992) 479–484.
- 703 [25] He, X. and Luo, L.S., A priori derivation of the lattice Boltzmann equation, *Phys. Rev. E*  
704 55 (1997) R6333.
- 705 [26] X. Shan, X. Yuan, H. Chen, Kinetic theory representation of hydrodynamics: a way beyond  
706 the Navier-Stokes equation., *J. Fluid Mech.* 550 (2006) 413–441.
- 707 [27] L. Zhong, S. Feng, P. Dong, S. Gao, Lattice Boltzmann schemes for the nonlinear Schrödinger  
708 equation., *Phys. Rev. E* 74 (2006) 036704.
- 709 [28] P. Romatschke, M. Mendoza, S. Succi, Fully relativistic lattice Boltzmann algorithm, *Phys.*  
710 *Rev. C* 84, doi:10.1103/PhysRevC.84.034903.
- 711 [29] P. Bhatnagar, E. Gross, M. Krook, A model for collision process in gases. I. Small amplitude  
712 process in charged and neutral one-component systems, *Phys. Rev.* 94(3) (1954) 511–525.
- 713 [30] D. d’Humières, I. Ginzburg, Y. Krafczyk, P. Lallemand, L. Luo, Multiple relaxation time  
714 lattice Boltzmann models in three dimensions, *Phil. Trans. R. Soc. Lon. A* 360 (2002) 437–  
715 451.
- 716 [31] S. Mari, D. Ricot, P. Sagaut, Comparison between Lattice Boltzmann Method and Navier-  
717 Stokes high order schemes for Computational Aeroacoustics., *J. Comput. Phys.* 228 (2009)  
718 1056–1070.
- 719 [32] Y. Peng, W. Liao, L.-S. Luo, L.-P. Wang, Comparison of the Lattice Boltzmann and pseudo-  
720 spectral methods for decaying turbulence: Low-order statistics, *Comp. & Fluids* 39 (4)  
721 (2010) 568 – 591, ISSN 0045-7930, doi:<https://doi.org/10.1016/j.compfluid.2009.10.002>,  
722 URL <http://www.sciencedirect.com/science/article/pii/S0045793009001546>.
- 723 [33] J. Sterling, S. Chen, Stability analysis of Lattice Boltzmann methods, *J. Comput. Phys.* 123  
724 (1996) 196–206.
- 725 [34] C. David, P. Sagaut, Structural stability of Lattice Boltzmann schemes, *Physica A* 444  
726 (2016) 1–8.

- 727 [35] C. Coreixas, G. Wissocq, B. Chopard, J. Latt, Impact of collision models on the  
728 physical properties and the stability of lattice Boltzmann methods, *Philosophical*  
729 *Transactions of the Royal Society A: Mathematical, Physical and Engineering Sci-*  
730 *ences* 378 (2175) (2020) 20190397, ISSN 1471-2962, doi:10.1098/rsta.2019.0397, URL  
731 <http://dx.doi.org/10.1098/rsta.2019.0397>.
- 732 [36] M. Geier, M. Schnherr, A. Pasquali, M. Krafczyk, The cumulant lattice Boltzmann equation  
733 in three dimensions: Theory and validation, *Computers and Mathematics with Applications*  
734 70 (4) (2015) 507 – 547, ISSN 0898-1221, doi:<https://doi.org/10.1016/j.camwa.2015.05.001>,  
735 URL <http://www.sciencedirect.com/science/article/pii/S0898122115002126>.
- 736 [37] J. Latt, B. Chopard, Lattice Boltzmann method with regularized pre-collision distribution  
737 functions, *Mathematics and Computers in Simulation* 72 (2) (2006) 165–168.
- 738 [38] F. Tosi, S. Ubertini, S. Succi, H. Chen, I. Karlin, Numerical stability of Entropic versus  
739 positivity-enforcing Lattice Boltzmann schemes, *Mathematics and Computers in Simulation*  
740 72 (2006) 227–231.
- 741 [39] P. Lallemand, F. Dubois, Some results on energy-conserving lattice Boltzmann models,  
742 *Computers and Mathematics with Applications* 65.
- 743 [40] F. Dubois, B. Graille, S. R. Rao, A notion of non-negativity preserving relaxation for a  
744 mono-dimensional three velocities scheme with relative velocity, *Journal of Computational*  
745 *Science* (2020) 101181ISSN 1877-7503, doi:<https://doi.org/10.1016/j.jocs.2020.101181>, URL  
746 <http://www.sciencedirect.com/science/article/pii/S1877750320304828>.
- 747 [41] C. Coreixas, B. Chopard, J. Latt, Comprehensive comparison of collision mod-  
748 els in the Lattice Boltzmann framework: Theoretical investigations, *Phys.*  
749 *Rev. E* 100 (3), ISSN 2470-0053, doi:10.1103/physreve.100.033305, URL  
750 <http://dx.doi.org/10.1103/PhysRevE.100.033305>.
- 751 [42] G.-H. Cottet, J.-M. Etancelin, F. Perignon, C. Picard, High order Semi-Lagrangian particles  
752 for transport equations: numerical analysis and implementation issues, *ESAIM: Mathemat-*  
753 *ical Modelling and Numerical Analysis* 48 (2014) 1029–1064.
- 754 [43] A. Magni, G.-H. Cottet, Accurate, non-oscillatory remeshing schemes for particle methods,  
755 *J. Comput. Phys.* 231(1) (2012) 152–172.
- 756 [44] G.-H. Cottet, P. Poncet, Advances in direct numerical simulation of 3D wall-bounded flows  
757 by Vortex-In-Cell methods, *J. Comput. Phys.* 193 (2003) 136–158.
- 758 [45] D.-G. Caprace, T. Gillis, P. Chatelain, FLUPS - A Fourier-based Library of Unbounded  
759 Poisson Solvers, *SIAM Journal on Scientific Computing* 43 (2021) [github.com/vortexlab-](https://github.com/vortexlab-uclouvain/flups)  
760 [uclouvain/flups](https://github.com/vortexlab-uclouvain/flups).
- 761 [46] R. Yokota, T. Narumi, R. Sakamaki, S. Kameoka, S. Obi, K. Yasuoka, Fast multipole  
762 methods on a cluster of GPUs for the meshless simulation of turbulence, *Comp. Physics*  
763 *Comm.* 180(11) (2009) 2066–2078.

- 764 [47] D. Rossinelli, B. Hejazialhosseini, W. M. van Rees, M. Gazzola, M. Bergdorf, P. Koumoutsakos, MRAG-I2D: Multi-resolution adapted grids for remeshed vortex methods on multicore  
765 architectures, *J. Comput. Phys.* 288 (2015) 1–18.  
766
- 767 [48] G. Novati, S. Verma, D. Alexeev, D. Rossinelli, W. van Rees, P. Koumoutsakos, Synchronisation through learning for two self-propelled swimmers, *Bioinspir. Biomim.* 12 (2017)  
768 036001.  
769
- 770 [49] P. Koumoutsakos, Multiscale flow simulations using particles, *Ann. Rev. Fluid Mechanics*  
771 37 (2005) 457–487.
- 772 [50] W. M. Van Rees, A. Leonard, D. Pullin, P. Koumoutsakos, A comparison of Vortex and  
773 pseudo-spectral methods for the simulation of periodic vortical flows at high Reynolds num-  
774 bers, *J. Comput. Phys.* 230(8) (2011) 2794–2805.
- 775 [51] Lallemand, P. and Luo, L.S., Theory of the lattice Boltzmann method: Dispersion, dissipa-  
776 tion, isotropy, Galilean invariance and stability, *Phys. Rev. E* 61(06).
- 777 [52] T. Février, Extension et analyse des schémas de Boltzmann sur réseau : les schémas à vitesse  
778 relative., Ph.D. thesis, Univerist de Paris-Saclay, 2015.
- 779 [53] O. Malaspinas, Increasing stability and accuracy of the lattice Boltzmann  
780 scheme: recursivity and regularization, arXiv e-prints arXiv:1505.06900URL  
781 <https://arxiv.org/abs/1505.06900>.
- 782 [54] Y. Feng, P. Sagaut, W.-Q. Tao, A compressible Lattice Boltzmann finite volume  
783 model for high subsonic and transonic flows on regular lattices, *Comp. & Fluids* 131  
784 (2016) 45 – 55, ISSN 0045-7930, doi:<https://doi.org/10.1016/j.compfluid.2016.03.009>, URL  
785 <http://www.sciencedirect.com/science/article/pii/S0045793016300652>.
- 786 [55] A. D. Rosis, K. H. Luo, Role of higher-order Hermite polynomials in the central-moments-  
787 based lattice Boltzmann framework, *Phys. Rev. E* 99 (1), doi:10.1103/physreve.99.013301,  
788 URL <https://doi.org/10.1103/physreve.99.013301>.
- 789 [56] J. J., M. O., S. P., A new hybrid recursive regularised BhatnagarGrossKrook collision model  
790 for Lattice Boltzmann method-based large eddy simulation, *Journal of Turbulence* 19 (11-12)  
791 (2018) 1051–1076, doi:10.1080/14685248.2018.1540879.
- 792 [57] F. Dubois, P. Lallemand, Towards higher order lattice Boltzmann schemes, *J. Stat. Mech.*  
793 2009, doi:10.1088/1742-5468/2009/06/P06006.
- 794 [58] S. Guo, Y. Feng, J. Jacob, F. Renard, P. Sagaut, An efficient lattice Boltzmann method for  
795 compressible aerodynamics on D3Q19 lattice, *J. Comput. Phys.* .
- 796 [59] He, Xiaoyi and Luo, L.S., Lattice Boltzmann Model for the Incompressible Navier-Stokes  
797 Equation, *J. Stat. Phys.* 88 (1997) 927–944.

- 798 [60] G. Wissocq, P. Sagaut, J.-F. Boussuge, An extended spectral analysis of the lattice Boltzmann method: modal interactions and stability issues, *J. Comput. Phys.* 380 (2019) 311–333, doi:10.1016/j.jcp.2018.12.015, URL <https://doi.org/10.1016/j.jcp.2018.12.015>.
- 801 [61] O. Hald, Convergence of Vortex methods II, *SIAM J. Num. Anal* 16 (1979) 726–755.
- 802 [62] J. Beale, A. Majda, Vortex methods II: high order accuracy in 2 and 3 dimensions, *Math. Comput.* 32 (1982) 29–52.
- 803
- 804 [63] C. Anderson, C. Greengard, On Vortex methods, *SIAM J. Num. Anal.* 22 (1985) 413–440.
- 805 [64] G.-H. Cottet, P. Koumoutsakos, *Vortex Methods - Theory and Practice*, Cambridge University Press, 2000.
- 806
- 807 [65] F. Gendre, D. Ricot, G. Fritz, P. Sagaut, Grid refinement for aeroacoustics in the lattice Boltzmann method: A directional splitting approach, *Phys. Rev. E* 96, doi:10.1103/PhysRevE.96.023311.
- 808
- 809
- 810 [66] G. Wissocq, J.-F. m. c. Boussuge, P. Sagaut, Consistent vortex initialization for the athermal lattice Boltzmann method, *Phys. Rev. E* 101 (2020) 043306, doi:10.1103/PhysRevE.101.043306, URL <https://link.aps.org/doi/10.1103/PhysRevE.101.043306>.
- 811
- 812
- 813
- 814 [67] L. Kovaszny, Turbulence in supersonic flow., *J. Aeronautical Science* 20 (1953) 657–682.
- 815 [68] M. Haussmann, S. Simonis, H. Nirschl, M. J. Krause, Direct numerical simulation of decaying homogeneous isotropic turbulence numerical experiments on stability, consistency and accuracy of distinct lattice Boltzmann methods, *International Journal of Modern Physics C* 30 (09) (2019) 1950074, doi:10.1142/S0129183119500748.
- 816
- 817
- 818
- 819 [69] P. Skordos, Initial and Boundary Conditions for the lattice Boltzmann Method., *Phys. Rev. E* 48 (6) (1993) 4823–4842.
- 820
- 821 [70] R. Mei, L.-S. Luo, P. Lallemand, D. dHumires, Consistent initial conditions for Lattice Boltzmann simulations, *Comp. & Fluids* 35 (8) (2006) 855 – 862, ISSN 0045-7930, doi:<https://doi.org/10.1016/j.compfluid.2005.08.008>, URL <http://www.sciencedirect.com/science/article/pii/S0045793005001477>.
- 822
- 823
- 824
- 825 [71] M. Brachet, D. Meiron, S. Orszag, B. Nickel, R. Morf, U. Frisch, Small-scale structure of the Taylor-Green vortex., *J. Fluid Mech.* 130 (1983) 411–452.
- 826
- 827 [72] G.-H. Cottet, Artificial Viscosity Models for Vortex and Particle Methods, *J. Comput. Phys.* 127 (1996) 199–208.
- 828
- 829 [73] A. K. Saha, Three-dimensional numerical simulations of the transition of flow past a cube, *Phys. Fluids* 16 (2004) 1630–1646.
- 830

- 831 [74] M. H. Khan, A. Sharma, A. Agrawal, Simulation of Flow Around a Cube at Moderate  
832 Reynolds Numbers Using the Lattice Boltzmann Method, *J. Fluids Eng.* 142 (1), ISSN  
833 0098-2202, doi:10.1115/1.4044821, URL <https://doi.org/10.1115/1.4044821>, 011301.
- 834 [75] J. P. Caltagirone, Sur l'int eraction fluide-milieu poreux : Application au calcul des efforts  
835 exerc es sur un obstacle par un fluide visqueux, *C. R. Acad. Sci. Paris* 318.
- 836 [76] P. Angot, C.-H. Bruneau, P. Fabrie, A penalization method to take into account obstacles  
837 in incompressible viscous flows, *Numer. Math.* 81 (1999) 497–520.
- 838 [77] C.-H. Bruneau, I. Mortazavi, Passive control of the flow around a square cylinder using  
839 porous media, *Int. J. Numer. Methods Fluids* 46 (2004) 415–433.
- 840 [78] C. Mimeau, G.-H. Cottet, I. Mortazavi, Direct numerical simulations of three-dimensional  
841 flows past obstacles with a Vortex penalization method, *Comp. & Fluids* 136 (2016) 331–347.
- 842 [79] S. Verma, G. Abbati, G. Novati, P. Koumoutsakos, Computing the force distribution on the  
843 surface of complex, deforming geometries using Vortex methods and Brinkman penalization,  
844 *Int. J. Numer. Methods Fluids* 85 (8) (2017) 484–501.
- 845 [80] C. Bernier, M. Gazzola, R. Ronsse, P. Chatelain, Simulations of propelling and energy  
846 harvesting articulated bodies via Vortex Particle-Mesh methods, *J. Comput. Phys.* 392  
847 (2019) 34–55.
- 848 [81] F. Morency, H. Beaugendre, F. Gallizio, Aerodynamic force evaluation for ice shedding  
849 phenomenon using Vortex in cell scheme, penalisation and level set approaches, *Int. J.*  
850 *Numer. Methods Fluids* 26(9–10) (2012) 435–450.
- 851 [82] Q. Zou, X. He, On pressure and velocity boundary conditions for the lattice Boltz-  
852 mann BGK model, *Phys. Fluids* 9 (6) (1997) 1591–1598, doi:10.1063/1.869307, URL  
853 <https://doi.org/10.1063/1.869307>.
- 854 [83] X. He, Q. Zou, L.-S. Luo, M. Dembo, Analytic solutions of simple flows and analysis of  
855 nonslip boundary conditions for the lattice Boltzmann BGK model, *Journal of Statistical*  
856 *Physics* 87 (1) (1997) 1572–9613, doi:10.1007/BF02181482.
- 857 [84] T. Inamuro, M. Yoshino, F. Ogino, A nonslip boundary condition for lattice Boltzmann  
858 simulations, *Phys. Fluids* 7 (12) (1995) 2928–2930, doi:10.1063/1.868766.
- 859 [85] J. Wu, C. Shu, An improved immersed boundary-lattice Boltzmann method for sim-  
860 ulating three-dimensional incompressible flows, *J. Comput. Phys.* 229 (13) (2010)  
861 5022 – 5042, ISSN 0021-9991, doi:<https://doi.org/10.1016/j.jcp.2010.03.024>, URL  
862 <http://www.sciencedirect.com/science/article/pii/S0021999110001348>.
- 863 [86] A. Haider, O. Levenspiel, Drag Coefficient and Terminal Velocity of Spherical and Non-  
864 spherical Particles, *Powder Technology* 58 (1989) 63–70.

865 [87] L. Klotz, S. Goujon-Durand, J. Rokicki, J. Wesfreid, Experimental investigation of flow  
866 behind a cube for moderate Reynolds numbers, *J. Fluid Mech.* 750 (2014) 7398, doi:  
867 10.1017/jfm.2014.236.

## Declaration of interests

- The authors declare that they have no known competing financial interests or personal relationships that could have appeared to influence the work reported in this paper.
- The authors declare the following financial interests/personal relationships which may be considered as potential competing interests:

The authors,  
Paris, 22th September 2020

le cnam

Conseatoire National des Arts et Métiers  
Laboratoire M2N  
2 Rue Conté  
75003 Paris, France

Credit Author statement

**Chloé Mimeau:** Conceptualization, Methodology, Software, Validation, Investigation, Resources, Writing (Draft and Review), Visualization.

**Simon Marié:** Conceptualization, Methodology, Software, Validation, Investigation, Resources, Writing (Draft and Review), Visualization.

**Iraj Mortazavi:** Conceptualization, Methodology, Investigation, Resources, Writing (Draft and Review).